Nonlinear rheology and dynamics of supramolecular polymer networks formed by associative telechelic chains under shear and extensional flows

Article

Accepted Version

It is advisable to refer to the publisher's version if you intend to cite from the work. See Guidance on citing.

To link to this article DOI: http://dx.doi.org/10.1122/1.5120897

Publisher: Society of Rheology

Nonlinear Rheology and Dynamics of Supramolecular Polymer Networks Formed by Associative Telechelic Chains Under Shear and Extensional Flows

Dipesh Amin and Zuowei Wang[1, a)]

School of Mathematical, Physical and Computational Sciences,

University of Reading, Whiteknights, PO Box 220, Reading RG6 6AX,

UK

Nonequilibrium computer simulations have been applied to study the shear and extensional flow behavior of supramolecular polymer networks (SPNs) formed by unentangled and weakly entangled associative telechelic chains and their non-associative polymer melt counterparts. The reversible bonding of the associative end monomers or stickers leads to the formation of percolated transient networks and consequently stronger mechanical properties of the SPNs than their melt counterparts. In startup shear the transient shear viscosities $\eta(t)$ and first normal stress coefficients $\Psi_1(t)$ of both the SPN and melt systems show overshoot behavior, but only the SPNs demonstrate transient strain hardening at high shear rates. In startup planar extensional flows all systems demonstrate the characteristic extensional strain hardening behavior. The transient extensional viscosities $\eta_E(t)$ of the SPNs undergo a small overshoot before entering the steady state, which was not observed in the non-associative polymer melts. For both types of polymer systems with unentangled and weakly entangled chain lengths, the steady-state shear viscosities show typical shear-thinning behavior, while the steady-state extensional viscosities demonstrate extension hardening, which are consistent with published simulation and experimental works. The observed flow behavior can be well understood from the flow-induced non-Gaussian chain stretching and segment orientation in all polymer systems studied, as well as the additional relaxation mechanisms in the SPNs, including the flow-induced reduction in the density of elastically active strands, the increment in the probability for the stickers to exchange their associated partners and at high strain rates the reduction in the average sticky bond lifetimes.

[a)]Electronic mail: zuowei.wang@reading.ac.uk

I.   INTRODUCTION

Supramolecular polymer networks (SPNs) formed by physically cross-linked polymers have attracted extensive attention due to their numerous potential applications, such as in developing materials with unique self-healing and stimuli-sensitive features [1–5]. The structural, dynamic and rheological properties of these transient networks are predominantly determined by the nature of the non-covalent interactions between the associating groups, also called stickers, and the compositions of the polymer chains, in particular the chemical distribution of the stickers on these molecules which lead to different relaxation mechanisms in the systems [6–20].

In supramolecular networks formed by linear polymers with multiple stickers per chain, each polymer is cross-linked with several other chains via a sequence of sticky bonds along its backbone. The sticky Rouse and sticky reptation models predict that the chain terminal relaxation time is proportional to the product of the renormalized sticky bond lifetime and either the square or cubic number of the interchain sticky bonds per chain, depending on whether the polymers are unentangled or entangled [21–23]. The renormalization of the bond lifetime takes into account the effect that a sticker needs to break and recombine with its old partner many times before finding a new partner to associate with. This renormalization picture has been verified in recent experimental [24] and computer simulation works [25 and 26]. It has also been suggested that the influence of hindered fluctuations should also be incorporated into the tube-based theoretical models for describing the dynamics of entangled SPNs [10].

On the other hand, telechelic polymers with end group stickers can associate into flower-like micelles in dilute or semidilute solutions which are bridged by single or linear sequence of polymer chains. The relaxation of such systems are proposed to proceed by single chain relaxation and much slower positional rearrangement of the micelles [16, 27–30]. At high concentrations, the stickers aggregate into clusters to cross-link the chains into transient networks with topological structures analogous to permanent polymer networks [26]. The simple architecture of telechelic polymers makes them good candidates for understanding the relaxation mechanisms of SPNs [8, 12, 13, 15–20, 31–35]. In the linear viscoelastic (LVE) regime, aqueous solutions of associative telechelic polymers, such as hydrophobically modified ethoxylated urethanes (HEUR), behave as Maxwell fluids with a single relaxation

time at low concentrations, but become non-Maxwellian with a broadened mode distribution at concentrations above a critical value (e. g., ~ 4 wt% for HEUR) [18, 27, and 31]. The Maxwellian to non-Maxwellian transition was interpreted as a result of the change in the transient network structures from sparse networks composed of long superbridge strands to dense networks constructed by cross-linked single chains [19, 30, and 32].

The steady-state shear viscosity, $\eta(\dot{\gamma})$, of dilute solutions of associative telechelic polymers undergoes a crossover from Newtonian to shear thickening and then to shear thinning behavior with increasing shear rate $\dot{\gamma}$ [8, 15, 16, 18, 19, 30–33, and 36]. The critical shear rate for the onset of shear thickening shifts to lower value with the increase of the sticky bonding energy ε and polymer concentration [8 and 15], while the magnitude of thickening increases with the increase of ε [15] but decreases with concentration [15 and 19]. The shear thickening behavior vanishes at high polymer concentrations where $\eta(\dot{\gamma})$ transitions directly from linear to shear thinning regime [15, 19, and 20]. Compared with shear flows, fewer studies have been reported on the extensional behavior of SPNs formed by telechelic polymers. In uniaxial filament stretching experiments the steady-state extensional viscosity, $\eta_E(\dot{\epsilon})$, of HEUR solutions was found to experience tension thickening at intermediate extensional rates $\dot{\epsilon}$ [16]. Beyond a critical strain the elongating samples will eventually break down or rupture [16]. Instability of transient telechelic polymer networks has also been observed in shear flow due to the formation of shear bands with increasing shear rate [37].

A number of relaxation mechanisms have been proposed to interpret the nonlinear behavior of SPNs [16, 18, 28, 30, 32, 38, and 39]. The free path (FP) model of Marrcucci *et al.* suggests that for transient polymer networks with constant number of elastically active strands the shear thickening behavior results from the non-Gaussian stretching of polymer chains under flow [28]. This chain stretching picture has been applied to explain both the shear thickening behavior [15] and the strain hardening of elastic modulus in step-strain experiments [40] of aqueous solutions of associative telechelic polymers. But experiments on semidilute solutions of unentangled polymers with multiple associating sites per chain suggested that the shear-induced transformation of intra-chain to inter-chain crosslinking, as proposed by Witten and Cohen [38], is the primary mechanism for shear thickening [8]. The application of intermediate shear rates to telechelic polymer systems may also lead to increment in the cross-linking density by converting dangling or looping chains to bridging strands [16, 32, and 41]. Tripathi *et al.* proposed a nonlinear two-species model

for associative telechelic polymers which takes into account the nonlinear chain extension, shear-induced enhancement of association and stretch-induced dissociation of stickers, and stress contributions from both the bridging and dangling chains [16]. With a tuneable constitutive parameter this model was able to describe the shear thickening and subsequent shear-thinning behavior of HEUR solutions, and also the transient extensional stress growth curves. The value of the tuning parameter is however not conveniently accessible in experiments. More recently Suzuki *et al.* observed in relatively dilute HEUR solutions that the shear thickening behavior is accompanied by the linear behavior of the first normal stress coefficient. They thus suggested that shear thickening arises from the enhanced reassociation rate in the shear gradient direction due to the anisotropic spatial distribution of the micellar cores in the superbridges [18 and 19]. In their systems, the network strands were only moderately stretched and so showed no significant finite extensible nonlinear elasticity effect. [18] So far experimental results obtained in different and sometimes even similar systems are giving inconsistent or even controversial nonlinear relaxation pictures, making it difficult for current theoretical models to describe various experimental observations consistently. To resolve this problem, direct evidences of the microscopic relaxation mechanisms in SPNs are highly desired, which could be achieved from computer simulations using atomistic or bead-spring associative polymer models.

Simulation studies on the nonlinear behavior of SPNs are much less than those on non-associative polymer melts[42–44]. The Brownian dynamics (BD) simulations of Cifre *et al.* used a simplified non-interacting dumbbell model and so missed nearly the entire relaxation spectrum of the polymer chains [41]. Li *et al.* performed molecular dynamics (MD) simulations of supramolecular polymer solutions under steady shear [45]. The short bead-spring chains they used can only undergo head-to-tail association, and the simulated systems demonstrated shear-thinning behavior. Hoy and Fredrickson developed a hybrid molecular dynamics/Monte Carlo (MD/MC) simulation method for studying the quiescent and nonequilibrium dynamics of supramolecular networks formed by unentangled chains each containing multiple binary associating sites [46]. The nonlinear mechanical properties they studied include the extension compliance in creep tests and stress-strain relation under constant volume tension. Recently Park and Ianniruberto developed a Brownian dynamics algorithm to simulate semidilute solutions of coarse-grained telechelic associating polymers where flowerlike micelles are bridged into 3D networks [34]. Their simulation results sug-

gested that the finite extensibility of the chains is mostly responsible for strain hardening in startup shear.

In this work we present nonequilibrium (NE) hybrid MD/MC simulations of the shear and extensional flow behavior of SPNs formed by associative telechelic polymers and their non-associative polymer melt counterparts. The telechelic polymers are represented by flexible bead-spring chains with one sticker at each chain end [26 and 47]. In previous equilibrium simulations [26], we have shown that above a critical sticky bonding energy, the stickers associate into clusters of finite sizes which cross link the telechelic chains into 3D percolated transient networks. The stress relaxation functions of the SPNs formed at high enough ε values demonstrate three relaxation regimes, i.e., initial Rouse, intermediate rubbery and terminal relaxation, in good consistence with recent experimental observations [20]. SPNs formed in melt condition are closely related to practical applications, such as self-healing materials, due to their strong mechanical properties and long-term stability. The NE simulation methods used for studying their nonlinear behavior are described in Sec. 2. Simulation results are presented and discussed in Sec. 3, and we draw conclusions in Sec. 4.

II.   SIMULATION METHODOLOGY

The hybrid MD/MC simulation method we employed is similar to that proposed by Hoy and Fredrickson [46] and has been described in details in a previous publication [26]. Here we present a brief summary. Both the associative telechelic and the non-associative polymers are represented by the flexible Kremer-Grest (KG) bead-spring chain model [47]. Each chain consists of N monomers with the monomer at each chain end defined as a sticker for the telechelic ones. The stickers are identical to normal monomers, except that they can reversibly associate with each other. Similar to previous work [26], the functionality of the stickers is fixed to $f = 3$ such that each of them can maximally bond with two other stickers. All monomers in a given system interact pairwise via the purely repulsive Lennard-Jones potential (LJ) potential, $U_{LJ}(r)$, with the cutoff distance $r_c = 2^{1/6}\sigma_{LJ}$ where σ_{LJ} is the monomer diameter and the LJ interaction parameter $\epsilon_{LJ} = 1.0k_BT$ where k_B and T are the Boltzmann constant and absolute temperature, respectively. Each pair of adjacent

5

monomers in a chain interact via the finitely extensible nonlinear elastic (FENE) potential

$$U_{FENE}(r) = -\frac{kR_0^2}{2} \ln \left[1 - \left(\frac{r}{R_0} \right)^2 \right] \tag{1}$$

where r is the center-to-center distance of the two monomers, $R_0 = 1.5\sigma_{LJ}$ and $k = 30\epsilon_{LJ}/\sigma_{LJ}$, respectively. The resulted statistical bond length of the flexible KG chain is $b = 1.32\sigma_{LJ}$. The time scales used in this work are all measured in the LJ time unit $\tau_{LJ} = \sqrt{m\sigma_{LJ}^2/\epsilon_{LJ}}$ with m the monomer mass. The monomer number density in all studied systems is fixed to $\rho = 0.85/\sigma_{LJ}^3$ as widely used in MD simulations of entangled polymer melts [47 and 48].

In the systems consisting of telechelic chains, two stickers that form a reversible sticky bond interact via the bonding potential [46 and 49]

$$U_{sb}(r, \varepsilon) = U_{FENE}(r) - U_{FENE}(r_0) - \varepsilon \tag{2}$$

where $r_0 \approx 0.97\sigma_{LJ}$ is the equilibrium FENE bond length at the minimum of the combined potential $U_{FENE}(r) + U_{LJ}(r)$. The energy offset $U_{FENE}(r_0) + \varepsilon$ in Eq.(2) is independent of r and so has no contribution to the bonding force. The sticky bonding energy ε determines the average lifetime of the sticky bonds. A Metropolis Monte Carlo algorithm is used to control the formation and breakage of the sticky bonds. The energy change due to formation of a new sticky bond is $\Delta E(r, \varepsilon) = U_{sb}(r, \varepsilon)$, while that for breaking an existing bond is $\Delta E(r, \varepsilon) = -U_{sb}(r, \varepsilon)$ [26 and 46]. At each MC step, pairs of stickers are chosen randomly by using a neighbor list built with a cut-off distance of $R_0 = 1.5\sigma_{LJ}$. If a chosen pair is already bonded, an attempt is made to break the bond. If they are not bonded, an attempt is made to create one between them. The successful rate of the trial moves is determined by the acceptance probability of $\min(1, \exp[-\Delta E(r, \varepsilon)/k_B T])$. These MC moves only involve changes in the topological connections between the stickers without altering their positions or momenta. The spatial motion of the monomers are all handled by integrating their equations of motion in the MD steps. On average each pair of stickers is chosen once per MC step, and any pair is allowed to be selected more than once during a MC step. For a given sticker, the formation/breakage of the $f - 1$ sticky bonds that it can form with other stickers are treated independently. The detailed balance condition is thus satisfied in our MC algorithm. This algorithm is used in both equilibrium and flow conditions based on the fact that the MC moves are only determined by the spatial separations between the stickers

6

not their velocities, even though rigorous proof of its mathematical foundation at high flow rates may still be needed.

The MC steps take place at a frequency of $\tau_{MC}/\delta t$ where δt is the MD time step size. The MC step size τ_{MC} governs the reaction kinetics of the sticky bonds. In our previous equilibrium simulations, an increase of τ_{MC} from $0.01\tau_{LJ}$ to $1\tau_{LJ}$ at fixed $\delta t = 0.01\tau_{LJ}$ was shown to have no influence on the static properties of the SPNs, but increase the average sticky bond lifetime and consequently the terminal relaxation times of the systems by a factor of about 100 (i.e., a factor linearly proportional to τ_{MC}) [26]. In this work we choose $\tau_{MC} = \tau_{LJ}$ which can also avoid potential spurious problems, such as temporal force discontinuities, caused by using too small MC step sizes (e.g., $\tau_{MC} \approx \delta t$) [46 and 49] although such spurious behavior was not observed in previous equilibrium simulations[26 and 46].

Before starting the nonequilibrium simulations, the polymer systems are first equilibrated as non-associative polymer melts by using standard MD simulations in quiescent state. Following that the sticker association mechanism is switched on in the telechelic chain systems which are then equilibrated for another time period by running the hybrid MD/MC simulations [26]. During the equilibration runs the trajectories of the monomers are determined by solving their Langevin equations of motion using the velocity Verlet algorithm with a MD time step size $\delta t = 0.01\tau_{LJ}$ [47, 48, and 50]. At each equilibration stage the simulation duration is multiple times of the terminal relaxation time of the corresponding system.

The nonlinear behavior of the model SPN and melt systems are studied under shear and planar extensional flows whose strain rate tensors are given as

$$\nabla \mathbf{u}_{shear} = \begin{pmatrix} 0 & 0 & 0 \\ \dot{\gamma} & 0 & 0 \\ 0 & 0 & 0 \end{pmatrix} \tag{3}$$

and

$$\nabla \mathbf{u}_{extension} = \begin{pmatrix} \dot{\epsilon} & 0 & 0 \\ 0 & -\dot{\epsilon} & 0 \\ 0 & 0 & 0 \end{pmatrix}. \tag{4}$$

Here $\dot{\gamma}$ and $\dot{\epsilon}$ denote the shear and planar extension rates, respectively. All of the NE simulations are carried out in the canonical (NVT) ensemble. For the shear flow simulations, we use a cubic simulation box and apply the Lees-Edwards "sliding brick" periodic boundary

conditions [50 and 51]. As defined in Eq.(3), the shear is along the $x-$axis and its gradient is along the $y-$axis. For the planar extensional flows, we employ the spatially and temporally periodic boundary conditions developed by Kraynik and Reinelt (KR) which allow the extension simulations to run for infinitely long time [52]. This method has been applied by Todd and Daivis to simulate various atomic and molecular fluids [43, 53, and 54]. Eq.(4) indicates that our simulation system elongates along the $x-$axis and contracts in the $y-$direction. The $z-$direction is intact in the planar extension flow.

In the MD steps of the NE simulations, the motion of the monomers is controlled by the SLLOD equations [50 and 55]

$$\dot{\mathbf{r}}_i = \frac{\mathbf{p_i}}{m_i} + \mathbf{r}_i \cdot \nabla \mathbf{u} \tag{5}$$

$$\dot{\mathbf{p}}_i = \mathbf{F}_i - \mathbf{p_i} \cdot \nabla \mathbf{u} - \zeta \mathbf{p_i} \tag{6}$$

where $\mathbf{F}_i$ is the sum of all the interaction forces acting on monomer i, including the non-bonded LJ and bonded FENE forces. $\mathbf{p}_i$ is the peculiar momentum of the monomer with respect to the streaming velocity $\mathbf{u}$. The thermostat multiplier ζ is given by Gaussian thermostat as [54 and 56]

$$\zeta = \frac{\sum_i \mathbf{p_i} \cdot (\mathbf{F}_i - \mathbf{p_i} \cdot \nabla \mathbf{u})}{\sum_i \mathbf{p_i}^2} + \zeta_0 \left[\frac{\sum_i \frac{\mathbf{p}_i^2}{m_i} - 3N_{tot}k_BT}{3N_{tot}k_BT} \right], \tag{7}$$

where N_{tot} is the total number of monomers in the system, and the second term is a proportional feedback term originally proposed by Baranyai *et al.* that counteracts the drift of the temperature [56]. The value of the weighting parameter ζ_0 should be sufficiently large to correct for the numerical drift, but not overwhelming to cause the equations of motion become stiff. In our simulations, the use of $\zeta_0 = 10$ is found to provide a stable temperature around the desired value. Eqs. (5) and (6) are solved numerically using the fourth order Gear predictor-corrector algorithm [50]. The MD time step size is chosen in the range of $\delta t = 0.002 - 0.005\tau_{LJ}$, depending on the strain rate. All NE simulations are performed using a simulation package developed in our group based on a GPU implementation.

The SLLOD equations conserve the total peculiar momentum of the system if it has been initialized to zero. In practice, the total momentum of each system is initialized to zero and any change in the total momentum is subtracted from the system at each time step to eliminate the arithmetic errors incurred in the numerical solution of the equations of motion.

In the absence of thermostat and at low Reynolds numbers, Daivis and Todd verified that the SLLOD equations of motion with proper implementation of boundary conditions can generate exactly the required dissipation of internal energy and consequently the correct adiabatic nonlinear responses for both shear and elongational flows [57]. But the use of different thermostats may have subtle effects on the nonlinear responses [43 and 58]. The Gaussian thermostat defined in Eq.(7) is the so-called atomic version which applies to each individual monomer, rather than to the center of mass of the whole molecule [43]. As will be shown in Section III, our simulation results obtained using Eqs.(5-7) on the steady-state shear and extensional viscosities of polymer melts agree with those generated by using different combinations of equations of motion and thermostats [42–44] and are also qualitatively consistent with relevant experimental works [59]. Daivis *et al.* have shown that for polymer melts consisting of unentangled bead-spring chains at low strain rates (below approximately 1), applying the SLLOD method with different thermostats can provide identical results [43]. Extension of the simulations to higher strain rates is restricted by the nature of the SLLOD method with the Gaussian thermostat [55] .Since all of our simulations are performed using the same set of equations of motion and thermostat, the results obtained from the SPN and melt systems can be compared with each other under the same numerical framework.

In this work we focus on the strongly associated supramolecular polymer networks by choosing the sticky bonding energy $\varepsilon = 10k_BT$. It has been shown in equilibrium simulations that the telechelic chains associate into 3D percolated transient networks at $\varepsilon > 4.3k_BT$ [26]. At $\varepsilon = 10k_BT$ the majority of the stickers are fully reacted (forming two sticky bonds for $f = 3$) and the fraction of open stickers is less than 1%. The stress relaxation function $G(t)$ also starts to demonstrate the rubbery feature at intermediate time scales, see also Fig.1. A further increase in ε (e.g., to $12 \sim 14k_BT$) will lead to exponential increase in the effective sticky bond lifetime and so the terminal relaxation time of the system [26]. As a consequence, much longer simulation runs will be needed for examining the proposed relaxation mechanisms which requires good statistics of the flow-induced sticker association/dissociation events, but no qualitatively different results are anticipated. We will leave the systematic study of $\varepsilon-$dependent flow behavior of SPNs for future work.

We choose to use two different polymer chain lengths, namely $N = 45$ and 128. In polymer melts consisting of flexible KG bead-spring chains, the entanglement strand length was estimated to be in the range of $N_e = 50 \sim 80$, depending on the analysis method used

[everaers04a,wangzw12a]. Therefore the short chains with $N = 45$ are unentangled, while the longer ones with $N = 128$ are weakly entangled with $Z \approx 1.6 \sim 2.6$ entanglements per chain. In the unentangled case, each simulation box contains $N_{ch} = 400$ chains that is twice the number of that used in our previous equilibrium simulations where the finite size effects was found to be insignificant [26]. All NE simulation results obtained at this chain length are averaged over 6 statistically independent runs. In the weakly entangled case, there are $N_{ch} = 150$ chains in the central simulation box and the results are averaged over at least 3 independent runs. For convenience, the non-associative polymer melts are simply called melts or melt systems in the remaining part of the paper.

III.   SIMULATION RESULTS AND DISCUSSIONS

In supramolecular polymer networks, the reversible bonding of the stickers gives rise to two characteristic times, namely the average sticky bond lifetime, τ_b, and the renormalized bond lifetime which in our model systems is the sticker partner exchange time, τ_{pe} [26]. In simulations, τ_b is calculated as the average time internal between the moment when a sticky bond is formed between two stickers and the moment when that bond breaks up, and τ_{pe} is calculated as the average time taken a sticker from being initially bonded with two partners to the moment of forming sticky bonds with two new partners. This definition of τ_{pe} has been justified for the stickers with functionality $f = 3$ [26].

In equilibrium simulations of the model SPNs with sticky bonding energy $\varepsilon = 10k_BT$, the two characteristic times are found to be $\tau_b^{eq} \approx 1.29 \times 10^3 \tau_{LJ}$ and $\tau_{pe}^{eq} \approx 2.18 \times 10^5 \tau_{LJ}$ at chain length $N = 45$, respectively. The partner exchange time τ_{pe}^{eq} has been shown to grow slowly with the chain length due to the resulted decrease in the sticker concentration [25 and 26], but this change is not significant for the two chain lengths studied in the current work at this relatively high ε, as reflected in the similar terminal relaxation times of the corresponding SPN systems. The terminal stress relaxation time of the SPNs with $N = 45$ is $\tau_{d,S}(N = 45) \approx 2.46 \times 10^5 \tau_{LJ}$ which is more than two orders of magnitude larger than that of their melt counterparts [$\tau_{d,M}(N = 45) \approx 1.21 \times 10^3 \tau_{LJ}$]. When the chain length is increased to $N = 128$, the terminal relaxation times are found to be $\tau_{d,S}(N = 128) \approx 2.63 \times 10^5 \tau_{LJ}$ for the SPNs and $\tau_{d,M}(N = 128) \approx 2.44 \times 10^4 \tau_{LJ}$ for the melts, respectively. The ratio of $\tau_{d,M}(N = 128)/\tau_{d,M}(N = 45)$ (≈ 20) is significantly larger than $(128/45)^2 \approx 8.1$ as expected

for the Rouse behavior, $\tau_R(N) \sim N^2$, indicating the entanglement effects in the systems of longer chains. On the other hand, $\tau_{d,S}(N = 128)$ is only slightly larger than $\tau_{d,S}(N = 45)$. This means that the terminal relaxation behavior of the SPNs is dominated by the reversible bonding of stickers, as also observed in experiments [20]. The Rouse time of well entangled polymer chains can be estimated using $\tau_R \approx \tau_e(N/N_e)^2$ where τ_e is the Rouse time of an entanglement strand of length N_e. Taking $\tau_e \approx 3290\tau_{LJ}$ and $N_e \approx 60$ as obtained by fitting the MD results on linear viscoelastic moduli to the Likhtman-McLeish theory [60 and 61]. τ_R of the flexible bead-spring chains with $N = 128$ is estimated to be around $1.5 \times 10^4\tau_{LJ}$. But this τ_R value could be overestimated, because the dynamics at such chain length is still in the crossover region from Rouse to entanglement behavior.

Fig. 1 presents the equilibrium simulation results on the stress relaxation function [61]

$$G(t) = \frac{V}{k_BT} \langle \sigma_{\alpha\beta}(t + t')\sigma_{\alpha\beta}(t') \rangle \tag{8}$$

and the orientational relaxation function

$$S(t) = \frac{1}{N_b k_B T} \left\langle \sum_{j=1}^{N_{ch}} O_j^{\alpha\beta}(t + t') \sum_{j=1}^{N_{ch}} O_j^{\alpha\beta}(t') \right\rangle \tag{9}$$

for the unentangled systems with chain length $N = 45$. Here $\sigma_{\alpha\beta}$ are the off-diagonal components of the stress tensor. $O_j^{\alpha\beta}(t) = \sum_{i=1}^{N-1} u_{ij}^\alpha(t)u_{ij}^\beta(0)$ is the orientation tensor of chain j, and $\mathbf{u}_{ij}$ is the ith bond vector of that chain. V and $N_b = N_{ch}(N-1)$ are the volume and total number of bonds in the system, respectively. The multiple-tau correlator method has been used to calculate $G(t)$ to ensure good statistics [62]. According to the stress-optical law, the stress and orientation tensors of a polymer system consisting of flexible chains are supposed to be proportional to each other in both the linear and nonlinear regimes as long as there is no strong chain stretching effect [63]. The results in Fig. 1 demonstrate that in equilibrium state this law is followed in both the melt and SPN systems via the relation of $G(t) = S(t)/Q$ where the stress-optical coefficient $Q = 0.0886(k_BT)^{-2}\sigma_{LJ}^3$, as used by Cao and Likhtman for polymer melts [61], works for both the associative and non-associative polymers we studied. The plateau-like region in $G(t)$ of the SPN indicates the transient network formation.
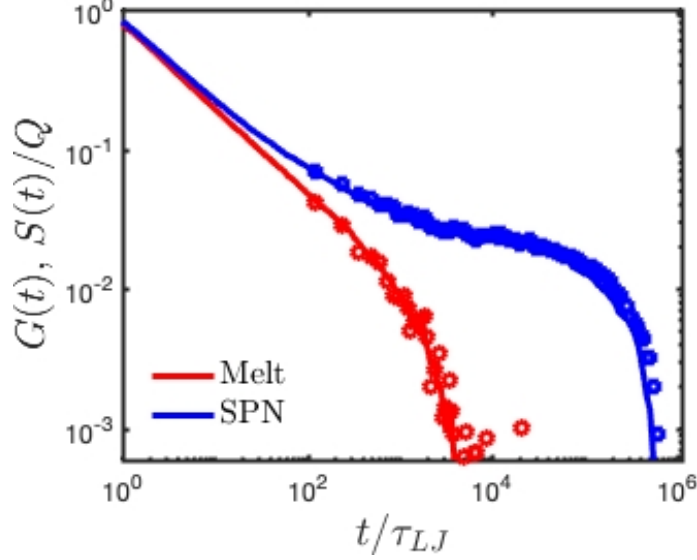
FIG. 1. Stress and orientation relaxation functions $G(t)$ (solid lines) and $S(t)$ (symbols) for the melt and SPN systems with chain length $N = 45$ obtained in equilibrium simulations. The $S(t)$ data have been divided by a constant $Q = 0.0886$ [61].

A. Startup shear

We begin the NE simulations with the startup shear of the SPN and melt systems. For entangled polymer melts, a stress overshoot behavior has been observed at shear rates $\dot{\gamma} > 1/\tau_d$ where τ_d is the terminal relaxation time of the melt. When $1/\tau_d < \dot{\gamma} < 1/\tau_R$, tube theories suggested that this overshoot can be attributed to the orientation of the tube segments along the shear direction [63–65]. This picture is supported by recent experiments [66] and computer simulations [61 and 67]. When $\dot{\gamma} > 1/\tau_R$ or the Rouse Weissenberg number $Wi_R = \dot{\gamma}\tau_R > 1$, contribution from shear-induced chain or tube stretching becomes important. The stretching effect may play a dominant role at much higher shear rates [68]. In the SPN systems, the characteristic sticky bond lifetimes τ_b and τ_{pe} could be on either side of τ_R, depending on the sticky bonding energy ε and polymer chain length N, which makes Wi_R not necessarily the intrinsic parameter for separating the different contributions to stress. Therefore our discussions will be mainly using the standard Weissenberg number $Wi = \dot{\gamma}\tau_d$ where τ_d is the terminal stress relaxation time of a given system. Wi_R will be briefly mentioned when discussing the weakly entangled melts with $N = 128$.

For the unentangled systems with $N = 45$ the dimensionless shear rates $\dot{\gamma}\tau_{LJ}$ are chosen

12

to be in the ranges of $[5 \times 10^{-5}, 10^{-2}]$ for the SPNs and $[5 \times 10^{-4}, 10^{-1}]$ for the melts, corresponding to the Wissenberg numbers $Wi_S (= \dot{\gamma}\tau_{d,S}) \in [12.3, 2460]$ and $Wi_M (= \dot{\gamma}\tau_{d,M}) \in [0.61, 121]$, respectively. The Wi_S values we employed fall well into the typical range applied in experiments [20]. No simulations were attempted at $Wi_S \leq 1$, because the required shear rates ($\dot{\gamma}\tau_{LJ} < 4.06 \times 10^{-6}$) are too small for our model SPN systems to reach steady state within affordable computational efforts. For the systems with $N = 128$, the dimensionless shear rates are varied over two decades from $\dot{\gamma}\tau_{LJ} = 10^{-4}$ to 10^{-2}, corresponding to $Wi_S \in [26.3, 2630]$ and $Wi_M \in [2.44, 244]$, respectively. Using the τ_R value estimated above, the Rouse Weissenberg number is in the range of $Wi_R \in [1.5, 150]$. The stress-optical law was found to work well up to $Wi_R = 5.75$ in previous startup shear simulations of polymer melts with $N = 256$ [61]. Similar to the unentangled case, the use of much smaller shear rates with $Wi_R \ll 1$ is not computationally practical for reaching the steady state.

In Fig. 2 we present simulation results on the transient shear viscosity [63]

$$\eta(t) = \frac{\sigma_{xy}(t)}{\dot{\gamma}} \tag{10}$$

and the first normal stress coefficient

$$\Psi_1(t) = \frac{\sigma_{xx}(t) - \sigma_{yy}(t)}{\dot{\gamma}^2} \tag{11}$$

for the unentangled systems with $N = 45$. For comparison we have also included the linear viscosities, $\eta^+(t)$, and linear first normal stress coefficients, $\Psi_1^+(t)$, calculated from the stress relaxation functions $G(t)$ of the two different systems obtained in our equilibrium simulations

$$\eta^+(t) = \int_0^t G(t')dt' \tag{12}$$

and

$$\Psi_1^+(t) = 2\int_0^t t'G(t')dt'. \tag{13}$$

The results for the weakly entangled systems with $N = 128$ are qualitatively very similar, see Fig.S1 in the Supplementary Material (SM).

Figs. 2(a,c) show that at short time scales or small shear strains $\gamma = \dot{\gamma}t$, the $\eta(t)$ and $\Psi_1(t)$ results of the melts agree with the LVE envelopes very well. This effectively validates the NEMD simulation method we implemented for studying shear flows. For the unentangled melts, both sets of data obtained at $\dot{\gamma}\tau_{LJ} \leq 10^{-3}$ or $Wi_M \leq 1$ show the typical linear viscoelastic behavior by following the master $\eta^+(t)$ and $\Psi_1^+(t)$ curves all the way into the
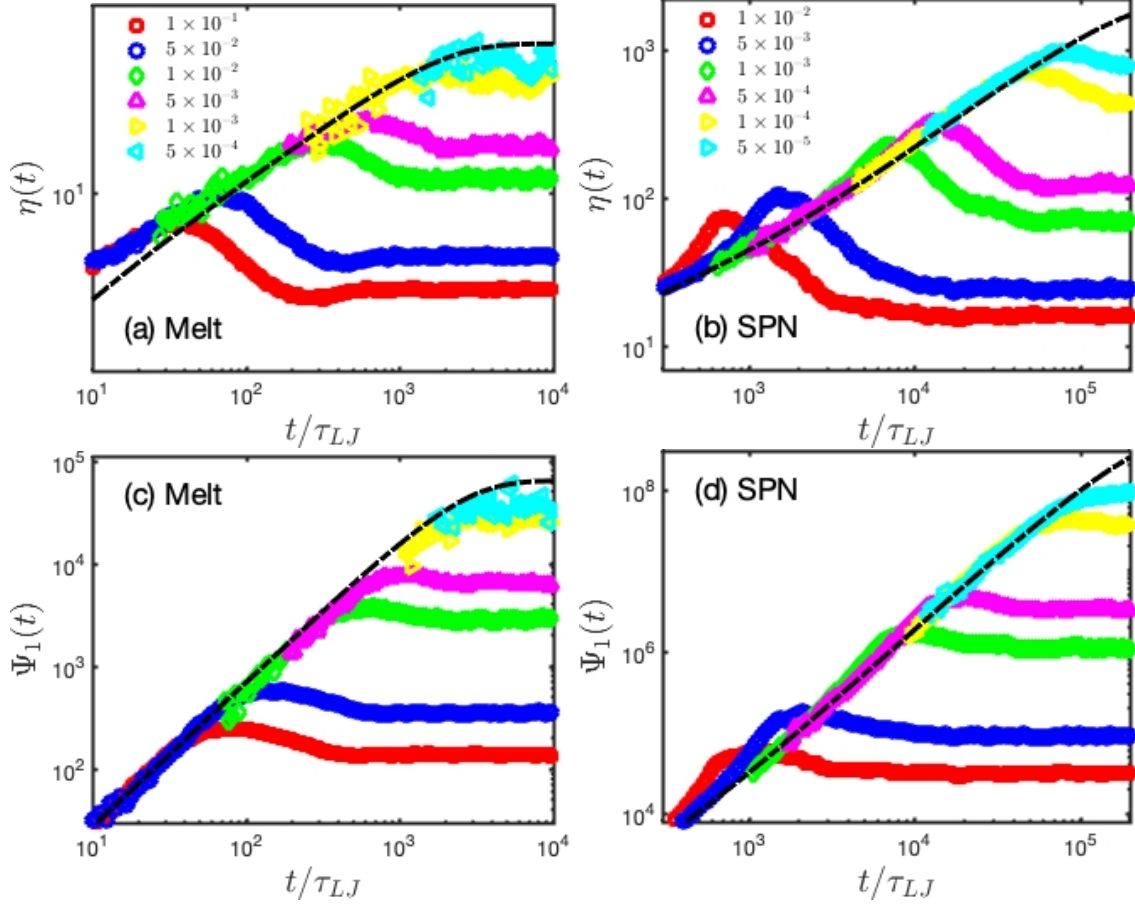
13

FIG. 2. Transient shear viscosities $\eta(t)$ and first normal stress coefficients $\Psi_1(t)$ obtained from startup shear simulations of the melts (a,c) and SPNs (b,d) with chain length $N = 45$ at different dimensionless shear rates $\dot{\gamma}\tau_{LJ}$. The black dot-dashed lines are the linear viscosities $\eta^+(t)$ and linear first normal stress coefficients $\Psi_1^+(t)$ calculated in equilibrium simulations of the corresponding systems.

steady state. The shear rates used for the weakly entangled systems with $N = 128$ are not low enough to demonstrate this linear behavior at longer times.

At higher $\dot{\gamma}$, the unentangled and weakly entangled melts show qualitatively very similar shear behavior, although the results in the latter systems are of higher magnitudes due to entanglement effects. Their shear viscosities demonstrate a clear overshoot behavior by first growing with the LVE envelope, passing through a maximum and then decreasing before reaching the steady state. At the two highest $\dot{\gamma}$ we applied, a stress undershoot is also found before entering the steady state. The transient shear stress undershoot has also been observed in entangled polymers in both experiments [69] and computer simulations [61]. The

physical origin of this undershoot was recently related to the chain tumbling behavior under shear [69]. Fig. 2(a) also shows that the height of the shear viscosity maximum decreases, but its ratio to the steady-state plateau value increases, with the increase of the shear rate. The shear strain at which the stress maximum occurs is found to be $\gamma_{max} \approx 2$ at small $\dot{\gamma}$ (e. g., $10^{-3}\tau_{LJ}^{-1}$), which is close to the theoretical prediction ($\gamma_{max} = 2$) of Doi and Edwards for entangled polymers at $Wi_M \geq 2$ [63], and then shifts to larger values with increasing $\dot{\gamma}$. The general increment trend of the height ($\sigma_{xy,max}$) and strain location (γ_{max}) of the shear stress maximum with $\dot{\gamma}$ can be seen more clearly in Fig. S5(a,c) of the SM for the melts with two different chain lengths, which is consistent with those found in experiments [70 and 71] and startup shear simulations using longer chains ($N = 512$) [61].

The overshoot behavior of the first normal stress coefficients $\Psi_1(t)$ of the melts appears at higher shear rates than that of $\eta(t)$. In experiments of entangled polymer melts this overshoot was considered to result from chain contour length elongation [70], which was not captured by the Doi-Edwards theory [63]. In the melts we studied, the maximum of the first normal stress, $\sigma_{xx}(t) - \sigma_{yy}(t)$, occurs at a larger shear strain than that of the shear stress $\sigma_{xy}(t)$ of the same sysem, but is of a lower relative magnitude as measured by the ratio between the maximum and steady-state values. These differences can be understood from the dependence of different stress tensor components on the chain stretching and segment orientation vectors as discussed later in relation to Fig. 3. There is no clear evidence of undershoot in our $\Psi_1(t)$ results.

The reversible association of the telechelic chains drastically enhances the viscoelastic properties of the supramolecular systems. As shown in Figs. 2(b,d), the $\eta(t)$ and $\Psi_1(t)$ results of the SPNs are significantly higher than those of their melt counterparts, especially at smaller shear rates where the transient networks contain higher density of elastically active strands and so generate rheological properties orders of magnitude stronger than the non-associative polymers. Similar to the melt systems, the $\eta(t)$ and $\Psi_1(t)$ data of the SPNs also behave linearly at very small shear strains and coincide with their LVE envelopes. The stress overshoot can be seen clearly in all of the $\eta(t)$ curves, and the overshoot in $\Psi_1(t)$ becomes evident at high shear rates. At a given $\dot{\gamma}$, the stress maximum of a SPN system happens at a larger strain γ_{max} than its melt counterpart, implying that the cross-linked chains can sustain higher extensions, see the shear stress-strain curves presented in Fig. S3 of the SM.

Qualitatively different from the melts, the peaks of the $\eta(t)$ and $\Psi_1(t)$ curves of the SPNs go above the LVE envelopes at high $\dot{\gamma}$, demonstrating a transient strain hardening behavior. The strain hardening is of larger relative magnitude in $\eta(t)$ than in $\Psi_1(t)$. Converting the $\eta(t)$ data into shear stress-strain curves $\sigma_{xy}(\gamma)$, our simulation results in Fig. S3(b) for the SPNs with $N = 45$ are found to be qualitatively consistent with the experimental data obtained from supramolecular networks formed by unentangled PIB-BA2 polymers [20]. Both sets of data show the increase of the height and strain location of the stress maximum with the increase of the shear rate, see also Fig. S5(a,b) of the SM. Quantitative comparison between the simulation and experimental results is however difficult due to different sticker association mechanisms and different sticky bond lifetimes involved in the studied systems.

The stress undershoot is not clearly visible in the $\eta(t)$ results of the SPNs in Fig.2(c) for $N = 45$ and Fig. S1(b) of the SM for $N = 128$. One possible reason is the suppression of chain tumbling due to the physical association of the chain sticky ends. The chain tumbling behavior in the steady state of the shear flows can be characterized by calculating the autocorrelation function $\Phi(t)$ of the unit end-to-end vectors of the polymer chains [72 and 73], see Section S3 in the SM. As shown in Fig. S6 there, $\Phi(t)$ of the unentangled melts with $N = 45$ obtained at $\dot{\gamma}\tau_{LJ} = 10^{-2}$ ($Wi_M = 12.1$) demonstrates a damped oscillatory behavior that after the initial monotonic decrease it passes below the zero axis and then rises above it with reduced amplitude until eventually decays to zero, indicating the existence of chain tumbling behavior. But much higher shear rates are needed for the chains to undergo periodic tumbling [72 and 73]. It is also not straightforward to relate the chain tumbling behavior in steady state to the stress undershoot in startup shear. On the other hand, up to the same shear rate (corresponding to $Wi_S = 2.46 \times 10^3$), it is hard to identify clear oscillation in $\Phi(t)$ of the corresponding SPNs. Similar behavior was observed in the SPNs with N = 128. These results imply that the chain tumbling behavior is suppressed by the transient network formation. For the SPNs studied in the current work, the majority of the stickers are still in the fully associated state over the simulated shear rate range, giving a relatively low fraction of dangling or free chains which have one or two end stickers unassociated. As shown in Fig. S7 of the SM, there are on average about 7.25% of dangling chains and 0.25% of free chains in the SPN system with $N = 45$ in the steady shear with $\dot{\gamma}\tau_{LJ} = 10^{-2}$. These dangling or free chains are typically short-lived, because the open stickers can quickly find nearby sticker clusters to associate with and the chains will turn back to the bridging state

with both ends associated. Therefore such non-bridging associative chains have very low likelihood to survive long enough to complete a tumbling circle, which differs significantly from the non-associative chains in the melt counterparts.
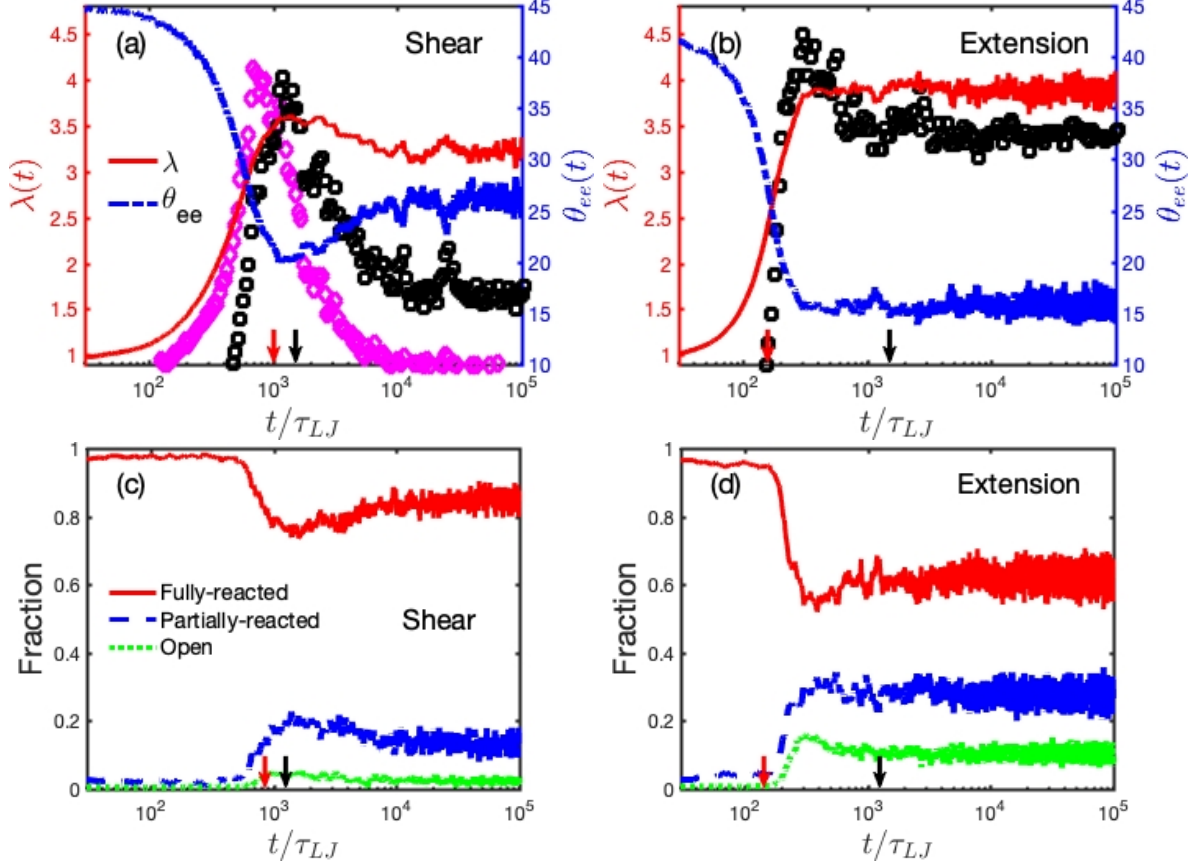

FIG. 3. (a, b) Average chain stretching ratio $\lambda(t)$, average chain end-to-end vector orientation angle with respect to the shear direction $\Theta_{ee}(t)$, and (c, d) average fractions of open, partially- and fully-reacted stickers as functions of time in the SPNs with chain length $N = 45$ under shear (a,c) and planar extensional flows (b,d). The strain rates are $\dot{\gamma} = \dot{\epsilon} = 10^{-2}\tau_{LJ}^{-1}$. Also included are the transient shear stress $\sigma_{xy}(t)$ (magenta diamonds) and first normal stress $\sigma_{xx}(t) - \sigma_{yy}(t)$ (black squares) in (a), and transient tensile stress $\sigma_{xx}(t) - \sigma_{yy}(t)$ (black squares) in (b). These stress data have been rescaled by multiplying some arbitrary numerical factors. In each plot, the short vertical arrows point to the average sticky bond lifetimes τ_b measured in equilibrium state (black arrows) and in the steady state of the shear or extensional flows (red arrows).

To further understand the startup shear behavior of the SPNs, we present in Fig. 3(a) the chain stretching ratio, $\lambda(t) \equiv R_{ee}(t)/R_{ee}^0$, where R_{ee} is the average chain end-to-end distance

17

at time t and $R^0_{ee} = N^{1/2}b$ is its equilibrium value, and the average orientation angle of the chain end-to-end vector with respect to the shear direction, $\Theta_{ee}(t)$, whose zero-shear value is $\Theta^0_{ee} = 45°$, for the SPN system with $N = 45$ at $\dot{\gamma}\tau_{LJ} = 10^{-2}$. The transient shear and normal stresses of the system are also included for convenience of discussion, which have been rescaled by multiplying some arbitrary numbers to make their maximum heights comparable to that of $\lambda(t)$. The increase of the chain stretching ratio happens simultaneously with the decrease of the chain orientation angle, and the two quantities reach their extreme values at the same time. The transient shear and normal stresses thus contain contributions from both shear-induced chain stretching and reorientation. A simple chain stretching force analysis below reveals that there is a non-Gaussian chain stretching contribution to the overshoot of the shear stress.

The force f_{stre} required to stretch a polymer chain to an end-to-end distance R_{ee} can be estimated by using the freely jointed chain model which gives [74]

$$\frac{f_{stre}b}{k_BT} \approx \mathcal{L}^{-1}\left(\frac{R_{ee}}{R_{max}}\right) \tag{14}$$

where the chain maximum extension is $R_{max} = (N-1)b$ and $\mathcal{L}(x) = \coth(x) - 1/x$ is the Langevin function. The inverse of the Langevin function can be calculated using the Cohen rounded Padé approximation [75 and 76]

$$\mathcal{L}^{-1}(x) = x\frac{3 - x^2}{1 - x^2}. \tag{15}$$

At weak chain stretching, Eq. (14) reduces to the Hooke's law for Gaussian chain

$$\frac{f_{gauss}b}{k_BT} \approx \frac{3R_{ee}}{R_{max}}. \tag{16}$$

For the bead-spring chains studied in this work, the actual stretching force may differ from the prediction of Eq.(14) by a constant prefactor c_f, which however will not affect the qualitative conclusions. Substituting the simulation results on $R_{ee}(t)$ into Eqs. (14) and (15) can provide estimation of the shear-induced chain stretching force as a function of time or strain. For the SPN studied in Fig. 3(a), the estimated stretching force at the maximum chain stretching ratio $\lambda_{max} \approx 3.09$ is $f_{stre} \approx 1.66c_fk_BT/b$ that is about 18.6% higher than the Gaussian force $f_{gauss} \approx 1.40c_fk_BT/b$ estimated using Eq. (16) at this λ. At the same shear rate, the maximum λ is around 1.82 in the melt counterpart and the corresponding relative difference between f_{stre} and f_{gauss} is only about 5.4%. The transient strain hardening

behavior in the SPN systems can thus be related to the shear-induced non-Gaussian chain stretching.

Fig. 3(a) further manifests the observation in Fig. 2 that the transient shear stress $\sigma_{xy}(t)$ reaches its maximum at earlier time or smaller strain than that for the first normal stress $\sigma_{xx}(t) - \sigma_{yy}(t)$, while the latter attains its maximum at nearly the same time as the chain stretching ratio $\lambda(t)$. Since the chain or segment stretching contribution becomes important when the shear and first normal stresses approach their maxima, these phenomena can be understood from the dependence of the diagonal and off-diagonal components of the stress tensor $\boldsymbol{\sigma}$ on the chain or segment stretching force $\mathbf{f}_{stre}$ and end-to-end vector $\mathbf{r}$, which on a molecular level can be calculated as $\sigma_{\alpha\beta} = \sum_i f_{stre,i\alpha} r_{i\beta}$ where $\alpha, \beta = (x, y, z)$ and the sum is over all chain segments [50 and 63]. In startup shear the polymer chains are getting more stretched and also more oriented along the shear (x-) direction, meaning that r_x and $f_{stre,x}$ grow with time, but r_y decreases with time. As a result the off-diagonal component $\sigma_{xy} \propto f_{stre,x} r_y$ reaches its maximum before the cross-linked chains are stretched to their maximum extension at the given $\dot{\gamma}$. But the diagonal component $\sigma_{xx} \propto f_{stre,x} r_x$ and so $\sigma_{xx} - \sigma_{yy}$ continue to grow until reaching their maxima simultaneously with chain stretching. The simulation results in Fig. 3(a) thus reflects a distinctive feature of the polymer systems under shear from those under extension where the tensile stress is only determined by the diagonal components of the stress tensor.

Fig. 3(c) shows the fractions of open, partially and fully reacted stickers (forming zero, one or two sticky bonds) in the SPN studied in Fig. 3(a) as functions of time. These fraction values remain roughly constant, implying the essentially unchanged topological structure of the transient network, up to a critical time scale that is comparable to the average sticky bond lifetime $\tau_b(\dot{\gamma})$ measured in the steady state of the shear flow (marked by red arrow). As will be seen in Sec. III C, $\tau_b(\dot{\gamma})$ is always smaller than the average sticky bond lifetime in equilibrium state τ_b^{eq} and decreases with increasing $\dot{\gamma}$. After this critical time the fraction of fully reacted stickers starts to drop quickly, accompanied by the increase in the fractions of partially-reacted and open stickers. There is thus a shear-induced reduction of the sticker association probability, which leads to a decrease of the number density of the bridging or elastically active strands in the transient network, e.g., see Fig. S7 in the SM. The parent polymers of the dissociated stickers will either work as dangling chains with one free end or as part of long linear strands consisting of two or more head-to-tail associated chains. They

become less stretched due to losing network connectivity and so release part of the stored stress. In the meantime, the remaining elastically active strands are still subject to affine-like non-Gaussian stretching under shear. Since the chain stretching ratio λ is averaged over all chains in the system, its value reaches the maximum when sufficiently large number of sticky bonds break up and the fraction of fully reacted stickers reaches its minimum. The magnitudes of the shear and first normal stresses are thus determined by the counter balance between the effects of the reduced number of elastically active strands due to sticky bond breakage and the continuously increasing stretching forces of the remaining active strands. Therefore the transient strain hardening behavior observed in the model SPNs mainly results from the shear-induced non-Gaussian stretching of the transient network strands, but not from the shear-induced enhancement of sticker associations. It is also noted in Fig. 3(c) that the majority of the stickers are still fully or partially associated even after entering the steady state. Correspondingly, up to 90% of the chains are in the bridging state at $\dot{\gamma}\tau_{LJ} \leq 1 \times 10^{-2}$, see Fig. S7 in the SM.

As will be shown in Sec. III C, the steady-state partner exchange time τ_{pe} decreases with the increase of the shear rate, but is still larger than τ_b over the entire range of $\dot{\gamma}$ we studied. It means that the effects of multiple breakage and recombination processes of the sticky bonds should still be taken into account for describing the nonlinear dynamics of the SPNs.

The free path model developed by Marrucci et $al.$ predicted that the unentangled telechelic chains in a transient network become fully stretched and so the shear thickening behavior starts at a critical shear rate $\dot{\gamma} \approx N^{1/2}/\tau$ where τ is the effective relaxation time of the chains in equilibrium state, $\tau \approx \frac{Nb^2}{a^2}\beta_0^{-1}$ [28]. The parameter β_0 is the detachment rate of a sticker from a sticker cluster and a is the average distance between the sticker clusters. Our previous equilibrium simulations of model SPNs have qualitatively validated the expression for τ by taking $\beta_0^{-1} \approx \tau_{pe}$ [26]. For the SPNs with $N = 45$, this theory predicts a critical shear rate $\dot{\gamma} \approx 2.73 \times 10^{-5}\tau_{LJ}^{-1}$ by substituting $\tau_{d,s}(N = 45)$ for τ. However, our simulation data in Fig. 3(a) show that the polymer chains are still far from being fully stretched, i.e., $\lambda_{max} \ll R_{max}/R_{ee}^0 \approx 6.7$, even at $\dot{\gamma}\tau_{LJ} = 10^{-2}$. The similar situation can also be found in Fig. 4 (b) for the weakly entangled SPNs with $N = 128$. Since the FP model was developed at a scaling level, the predicted critical shear rate may be subject to a numerical factor correction for comparing with those found in experiments or simulations. Another important issue is that the assumption of a fixed fraction of associated stickers in
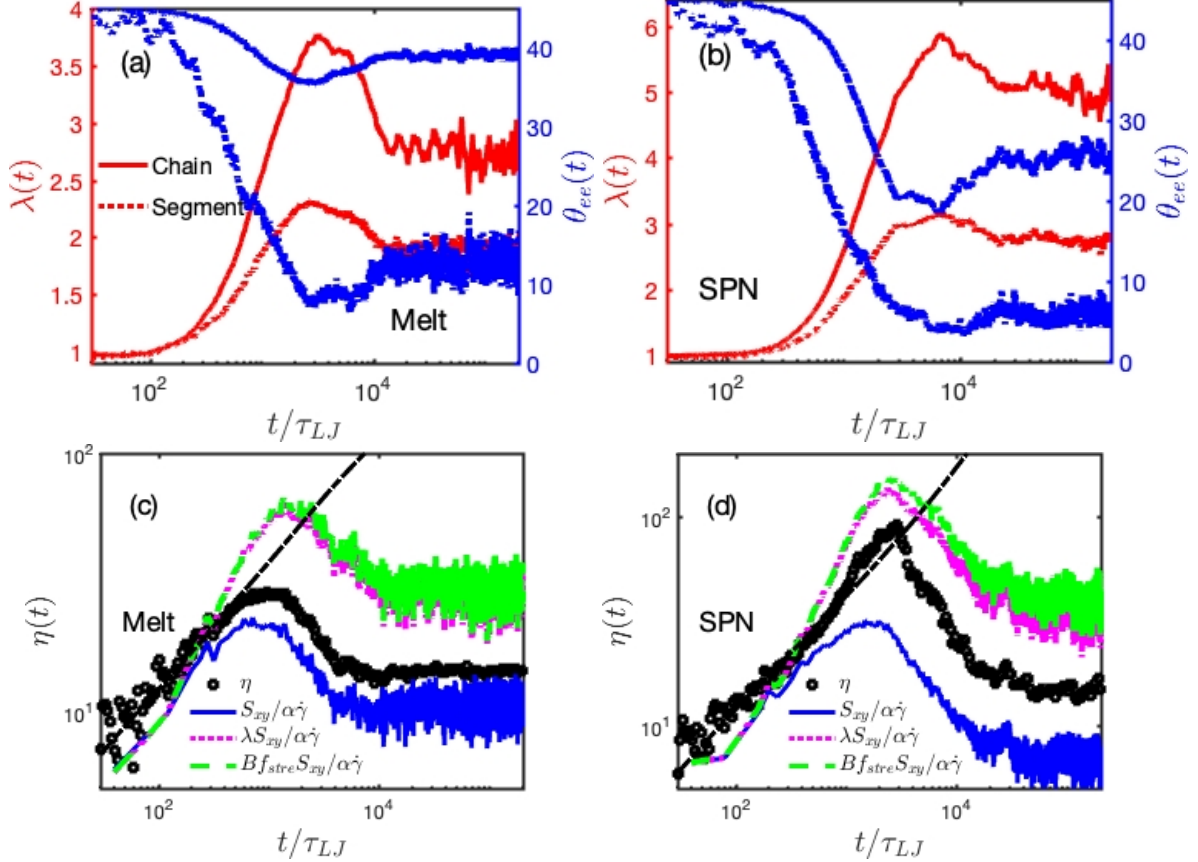
FIG. 4. (a,b) Average stretching ratios $\lambda(t)$ and end-to-end vector orientation angles $\Theta_{ee}(t)$ of both the entire chains (solid lines) and the chain segments of length $N_{seg} = 25$ (dashed lines), and (c,d) transient shear viscosities $\eta(t)$ in the melt and SPN systems with $N = 128$ at $\dot{\gamma}\tau_{LJ} = 5 \times 10^{-3}$. Also included in (c,d) are the shear viscosities estimated using three different approaches, i.e., the stress-optical law (blue solid), Eqs. 18 (magenta dashed) and 19 (green dashed), respectively. The black dashed lines are the linear viscosities $\eta^+(t)$ calculated in equilibrium simulations.

the FP model does not apply to our model SPNs over the range of shear rates we studied, as shown in Fig. 3(c) and later in Sec. III C via the flow-induced reduction in the fraction of fully associated stickers.

We use the polymer systems with longer chains to analyse the contributions of chain stretching and segment orientation to the shear stress tensor. Figs. 4(a,b) present the simulation results on $\lambda(t)$ and $\Theta_{ee}(t)$ for the systems with $N = 128$ at $\dot{\gamma}\tau_{LJ} = 5 \times 10^{-3}$. Together with them are the same structural quantities calculated for the chain segments of length $N_{seg} = 25$ in the same systems, for which we have only averaged over the middle 50

monomers of each chain to reduce the influence from the chain ends. For the melt system in Fig. 4(a), the maximum chain stretching ratio is $\lambda_{max} \approx 3.62$. The corresponding stretching force $f_{stre} \approx 1.04 c_f k_B T/b$ as estimated using Eq.(14) is 8.3% larger than the Gaussian force predicted by Eq.(16), indicating a rather weak non-Gaussian chain deformation at this shear rate ($Wi_M \approx 122$ or $Wi_R \approx 75$). The chain end-to-end vectors are also only weakly orientated along the shear direction with a minimum orientation angle $\Theta_{ee} \approx 36°$. On the other hand, the segments in the middle of the polymer chains show significantly smaller stretching ratio, but much stronger re-orientation with the minimum orientation angle smaller than $10°$.

In Fig. 4(c) simulation results on the transient shear viscosity $\eta(t)$ of the melt system are plotted together with the rescaled xy-component of the orientation tensor

$$S_{xy}(t) = \frac{1}{N_b} \sum_{j=1}^{N_{ch}} O_j^{xy}(t). \tag{17}$$

According to the stress-optical law, the shear stress is proportional to $S_{xy}(t)$ as $\sigma_{xy}(t) = S_{xy}(t)/\alpha$ where $\alpha = \sqrt{Q/\rho_b} \approx 0.32(k_B T)^{-1} \sigma_{LJ}^3$ for the flexible bead-spring chain model with bond density $\rho_b \approx 0.85 \sigma_{LJ}^{-3}$ and Q is the fitting parameter used in the equilibrium state, see Fig.1 [61]. The $S_{xy}(t)/\alpha\dot{\gamma}$ data show qualitatively very similar time-dependent behavior to the simulation results on $\eta(t)$. The two sets of data agree reasonably well in the linear regime, but the stress-optical law underestimates $\eta(t)$ at time scales close and beyond the stress maximum. The quantitative difference between them can be attributed to the contribution of non-Gaussian chain stretching.

In the startup shear, the SPNs effectively behave as permanent polymer networks before reaching the average bond lifetime at the given shear rate. When being plotted as functions of shear strain γ, both $\lambda(\gamma)$ and $\Theta_{ee}(\gamma)$ demonstrate the affine-like behavior by collapsing onto universal growing or decaying curves, regardless of the applied shear rates. Deviation from this universal behavior happens when the fraction of fully reacted stickers and consequently the number density of elastically active strands begin to decrease at critical strain values which increase with increasing $\dot{\gamma}$. The initial growth rates and the maximum values of the chain stretching ratios in the SPNs are significantly higher than those in their melt counterparts. As shown in Fig. 4(b), the maximum λ of the SPN is about 5.67 at which the chain stretching force f_{stre} ($\approx 1.85 c_f k_B T$) is about 22.6% higher than the estimated Gaussian force. This non-Gaussian stretching can be directly related to the transient strain hardening

22

behavior shown in Fig. 4(d). There the rescaled orientation tensor $\sigma_{xy}(t)$ demonstrates the overshoot behavior, but does not go beyond the LVE envelope, similar to that happens in the melt case in Fig. 4(c). The strain hardening in startup shear of SPNs thus originates from the non-Gaussian chain stretching rather than the chain segment orientation.

In early theoretical models for describing the flow behavior of entangled polymers, the chain stretching and segment orientation contributions to the shear or extensional stress were often treated as decoupled from each other [77 and 78]. Following this approach, the shear stress can be approximated by a product of the chain tension and the orientation tensor. As a first order approximation, the tension of unentangled or barely entangled polymers under shear is linearly proportional to the chain stretching ratio λ, giving the estimated shear stress

$$\tilde{\sigma}_{xy}(t) = A\lambda(t)S_{xy}(t)/\alpha \tag{18}$$

where the coefficient A can be taken as unity, because in Fig. 4(c) the stress-optical law is shown to work in the linear regime around $\lambda \approx 1$. To take into account the non-Gaussian chain stretching effect, the chain tension contribution in Eq.18 can be replaced by the non-linear stretching force estimated by Eqs.14 and 15 to give

$$\tilde{\sigma}_{xy}(t) = Bf_{stre}(t)S_{xy}(t)/\alpha \tag{19}$$

which should reduce to Eq.18 in the linear regime by setting $B = \frac{N^{1/2}}{3}(k_BT)^{-1}\sigma_{LJ}$. Using our simulation data on $\lambda(t)$ and $S_{xy}(t)$ as input, the predictions of Eqs. 18 and 19 on the transient shear viscosities $\tilde{\sigma}_{xy}(t)/\dot{\gamma}$ are shown in Fig. 4(c,d). Owing to the non-Gaussian chain stretching behavior in the studied systems, Eq.19 predicts stress values higher than those of Eq. 18 at large time scales. They are both significantly higher than the simulation data on $\eta(t)$. Moreover, these approximations predict an unphysical transient strain hardening behavior for the melt. The decoupling approximations and the simulation results on the steady-state shear viscosities $\eta(\dot{\gamma})$ are compared in Fig. S10(a) of the SM where their discrepancies get smaller at high shear rates due to strong chain stretching. These comparisons indicate that the coupling effect between the chain stretching and segment orientation contributions should be considered carefully in theoretical description of the flow behavior of polymer systems.
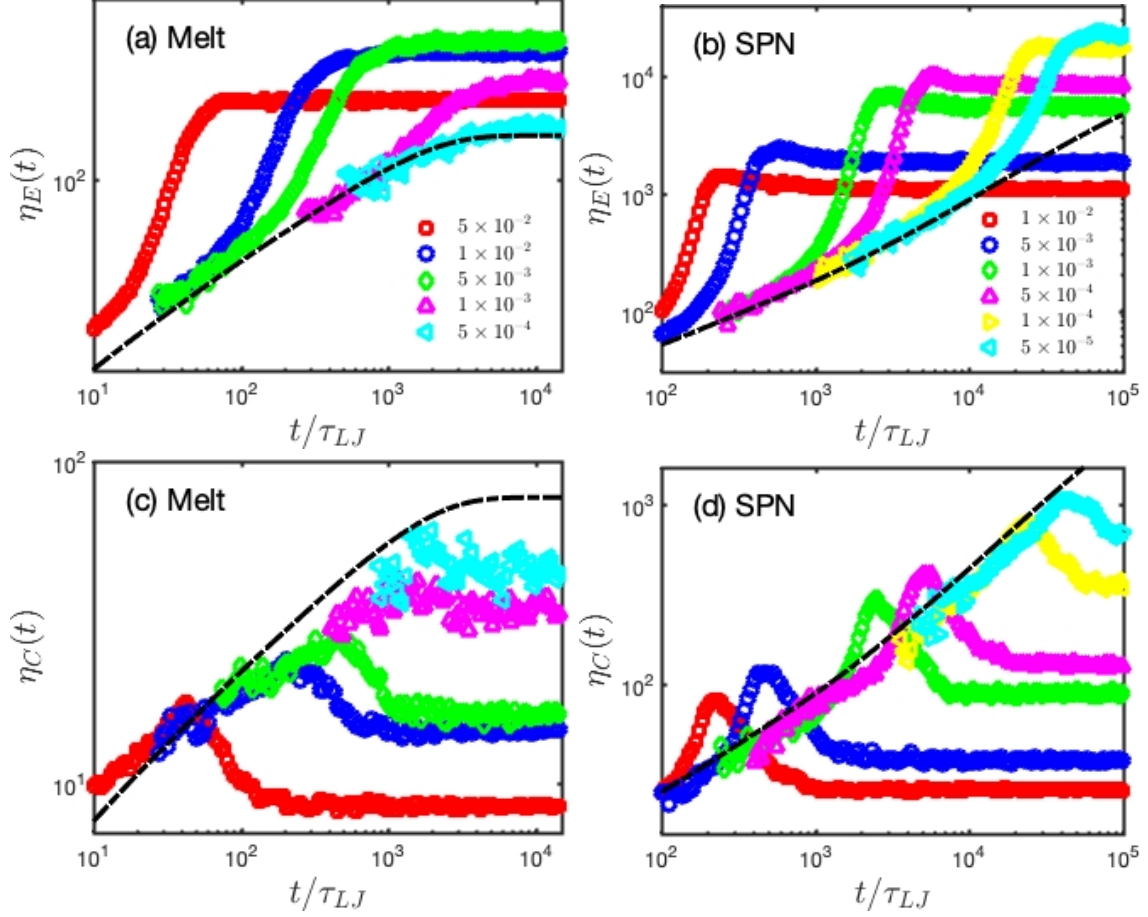
FIG. 5. Transient planar extensional viscosities $\eta_E(t)$ and cross viscosities $\eta_C(t)$ obtained from planar extension simulations of the melt (a,c) and SPN (b,d) systems with chain length $N = 45$ at different dimensionless extension rates $\dot{\epsilon}\tau_{LJ}$. The black dot-dashed lines represent the linear planar extensional and cross viscosities estimated as $Tr\eta^+(t)$ with the Trouton ratios $Tr = 4$ for $\eta_E(t)$ and 2 for $\eta_C(t)$.

B. Startup Planar Extension

The strain rates we applied in the planar extension simulations are very close to those used in the shear flow simulations. For the unentangled systems with chain length $N = 45$, the dimensionless extension rates are chosen to be $\dot{\epsilon}\tau_{LJ} \in [5 \times 10^{-5}, 10^{-2}]$ for the SPNs and $\dot{\epsilon}\tau_{LJ} \in [5 \times 10^{-4}, 5 \times 10^{-2}]$ for the melts, corresponding to Weissenberg numbers $Wi_S \in [12.3, 2460]$ and $Wi_M \in [0.605, 60.5]$, respectively. Those for the weakly entangled systems with $N = 128$ are $\dot{\epsilon}\tau_{LJ} \in [5 \times 10^{-5}, 5 \times 10^{-3}]$ ($Wi_S \in [13.2, 1320]$) for the SPNs and $\dot{\epsilon}\tau_{LJ} \in [5 \times 10^{-5}, 10^{-2}]$ ($Wi_M \in [1.22, 244]$), respectively.

24

The off-diagonal components of the stress tensor vanish in planar extension flows. Two transient extensional viscosities can be defined [79], i.e., the planar extensional viscosity

$$\eta_E(t) = \frac{\sigma_{xx}(t) - \sigma_{yy}(t)}{\dot{\epsilon}} \qquad (20)$$

which refers to the tensile stress required to stretch the material in the elongation (x-) direction, and the cross viscosity

$$\eta_C(t) = \frac{\sigma_{zz}(t) - \sigma_{yy}(t)}{\dot{\epsilon}}, \qquad (21)$$

which refers to the tensile stress required to prevent deformation in the neutral (z-) direction. The cross viscosity was rarely measured in experiments. One example could be found in the the study of strain hardening behavior of linear and branched polyolefin melts in extensional flows [80].

Fig. 5 presents the simulation results on $\eta_E(t)$ and $\eta_C(t)$ for the melt and SPN systems with chain length $N = 45$, together with their linear viscosities $\eta^+(t)$ which has been multiplied by the Trouton ratios ($Tr = 4$ for $\eta_E(t)$ and 2 for $\eta_C(t)$) between the planar extensional and shear viscosities of Newtonian fluids [79]. Qualitatively similar results have been obtained for the systems with $N = 128$, see Fig. S2 in the SM. At very small strains ϵ ($= \dot{\epsilon}t$), the $\eta_E(t)$ and $\eta_C(t)$ data follow the LVE curves reasonably well. Considering the good agreement of the transient shear viscosities $\eta(t)$ with $\eta^+(t)$ at small shear strains γ (Fig. 2 and Fig. S1 in the SM), the Trouton ratios of Newtonian fluids can be well used to describe the relation between the transient planar extensional and shear viscosities in the linear regime for all of the melt and SPN systems we studied. In Fig. 5(a), only $\eta_E(t)$ of the melts obtained at the smallest extension rate $\dot{\epsilon}\tau_{LJ} = 5 \times 10^{-4}$ follows the LVE envelope all the way into the steady state. At higher $\dot{\epsilon}$, the melt systems demonstrate clear transient strain hardening behavior with their planar extensional viscosities $\eta_E(t)$ going above the LVE data and then transitioning smoothly to the steady-state plateaus. Their transient cross viscosities $\eta_C(t)$ in Fig. 5(c) show overshoot behavior but no strain hardening, which is qualitatively similar to the $\eta(t)$ and $\Psi_1(t)$ data in Figs. 2(a,c). The reason may lie in that for non-associative polymer melts chain relaxation in the neutral (z-) direction is not strongly perturbed by the planar extension flow.

The extensional viscosities of the SPNs in Fig. 5(b,d) are much higher than those of their melt counterparts. The strong transient extensional strain hardening has also been

observed experimentally in supramolecular networks formed by entangled polymers with multiple associating groups per chain [81]. Fig. 5 reveals two qualitative differences of the startup extensional behavior of the SPNs from the non-associative melts. One is the transient strain hardening of the cross viscosities $\eta_C(t)$, which is similar to the $\eta(t)$ and $\Psi_1(t)$ data of the SPNs in Figs. 2(b,d). The other is the small overshoot in the planar extensional viscosities $\eta_E(t)$ before entering the steady state. The time required to reach the maximum of $\eta_E(t)$ decreases with the increase of the extension rate. Such an overshoot behavior was theoretically predicted by Tripathi et $al.$ for $\eta_E(t)$ of 4% HEUR solutions in uniaxial extensional flows with high Deborah numbers $De = \tau_E \dot{\epsilon}$ (e.g., $De = 9$) [16]. τ_E was defined as the characteristic time for a sticker to exit from an associated sticker cluster. If we use the equilibrium sticker partner exchange time τ_{pe}^{eq} for τ_E, the lowest extension rate we used ($\dot{\epsilon}\tau_{LJ} = 5 \times 10^{-5}$) corresponds to $De = \dot{\epsilon}\tau_{pe} \approx 10.9$. The extension rates applied in our simulations thus fall into the theoretical De range predicted for observing the overshoot behavior, although our supramolecular networks are formed in the melt condition.

In Fig. 3 (b) simulation results on the chain stretching ratio $\lambda(t)$ and orientation angle $\Theta_{ee}(t)$ of the unentangled SPNs at $\dot{\epsilon}\tau_{LJ} = 10^{-2}$ are plotted together with the rescaled transient tensile stress $\sigma_{xx}(t) - \sigma_{yy}(t)$. Similar to the first shear normal stress given in Fig.3 (a), the tensile stress undergoes an overshoot and reaches its maximum at the same time when $\lambda(t)$ and $\Theta_{ee}(t)$ enter their plateau regions. This can be attributed to the absence of the rotational components in the extensional deformation tensor. The plateau or steady-state value of λ is about 3.97, corresponding to a chain stretching force of $f_{stre} \approx 2.46 c_f k_B T/b$ as estimated using Eq.(14) which is 37.1% higher than the estimated Gaussian force. This again verifies the important role of non-Gaussian chain stretching in the transient strain hardening. The drop of the transient tensile stress from its maximum before entering the steady state can be clearly related to the decrease in the fraction of fully reacted stickers by about 20%, as shown in Fig. 3(d). This effectively reduces the number density of elastically active strands in the system. Compared with the startup shear results obtained at the same strain rate ($\dot{\gamma} = \dot{\epsilon}$) in Figs. 3 (a,c), the maximum λ and Θ_{ee} values in the extensional case are both significantly higher, leading to larger steady-state extensional viscosities $\eta_E(\dot{\epsilon})$ than the steady-state shear viscosities $\eta(\dot{\gamma})$.

Figs. 6(a, b) show the simulation results on $\lambda(t)$ and $\Theta_{ee}(t)$ of both the entire chains and the segments in the middle of the chains for the melt and SPN systems with $N = 128$ at
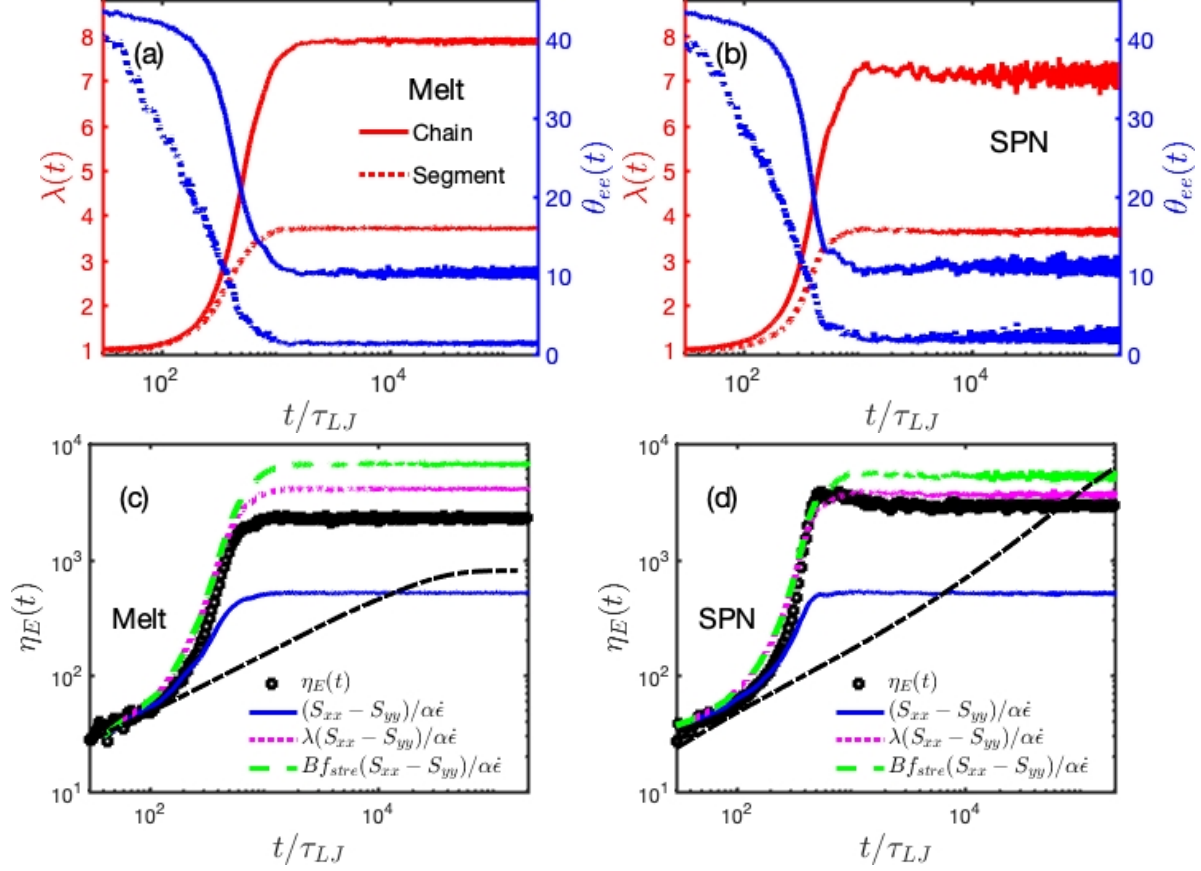
FIG. 6. (a,b) Average stretching ratios $\lambda(t)$ and end-to-end vector orientation angles $\Theta_{ee}(t)$ of both the entire chains (solid lines) and the chain segments of length $N_{seg} = 25$ (dashed lines), and (c,d) transient planar extensional viscosities $\eta_E(t)$ in the melt and SPN systems with $N = 128$ at dimensionless extension rate $\dot{\epsilon}\tau_{LJ} = 5 \times 10^{-3}$. Also included in (c,d) are the extensional viscosities estimated using three different approaches, i.e., the stress-optical law (blue solid), Eqs. 18 (magenta dashed) and 19 (green dashed) by replacing $\tilde{\sigma}_{xy}(t)$ and $S_{xy}(t)$ with $\tilde{\sigma}_{xx}(t) - \tilde{\sigma}_{yy}(t)$ and $S_{xx}(t) - S_{yy}(t)$, respectively. The black dashed lines are the linear planar extensional viscosities calculated as $\eta_E^+(t) = 4\eta^+(t)$.

$\dot{\epsilon}\tau_{LJ} = 5 \times 10^{-3}$ ($Wi_M = 122$ and $Wi_S = 1.32 \times 10^3$). It is noted that at this extension rate the flow-induced chain or segment stretching and reorientation behavior are of similar magnitudes in the two different systems. The chain stretching ratios are getting close to their maximum of $R_{max}/R_{ee}^0 \approx N^{1/2} \approx 11.3$ and the middle segments of the chains are nearly fully aligned with the elongation direction with $\Theta_{ee}(t) \sim 0$. Simulation results obtained at smaller $\dot{\epsilon}$ show qualitatively very similar but quantitatively weaker extensional behavior.

The transition of chain conformation from random coil to nearly straight configuration with increasing extension rate has also been observed in the simulations of entangled polymers by O'Connor *et al* [44]. In Figs. 6 (a,b) there are no obvious intermediate overshoot or undershoot regions before entering the steady state. If plotted as functions of the extension strain, the initial growth (or decaying) rate and the plateau value of $\lambda(t)$ (or $\Theta_{ee}(t)$) in the melts increase with increasing $\dot{\epsilon}$. In contrast, the chain or segment stretching and reorientation data in the SPNs demonstrate the initial affine-like behavior by collapsing onto universal steeply growing or decaying curves, and then deviate from them at earlier strain if subject to lower extension rate.

Figs. 6(c,d) examine the stress-optical law by plotting the rescaled differences between two diagonal components of the orientation tensor, $(S_{xx}(t) - S_{yy}(t))/\alpha\dot{\epsilon}$ with $\alpha = 0.32$, against the simulation data on $\eta_E(t)$. For each system the two sets of data show good agreement in the initial growing regime even above the LVE curve, but the steady-state plateau predicted by the stress-optical law is much lower than that of $\eta_E(t)$. The quantitative difference between them arises from the contributions of non-Gaussian chain stretching. Different from the startup shear results in Fig.4(b,d), the contributions from flow-induced segment orientation alone are strong enough to cause the transient extensional strain hardening. If the chain stretching and segment orientation contributions are assumed to be decoupled, the extensional tensile stresses can be estimated by replacing $\tilde{\sigma}_{xy}(t)$ and $S_{xy}(t)$ in Eqs. 18 and 19 with $\tilde{\sigma}_{xx} - \tilde{\sigma}_{yy}(t)$ and $S_{xx}(t) - S_{yy}(t)$, respectively. Using simulation data on $\lambda(t)$, $S_{xx}(t)$ and $S_{yy}(t)$ as input, the resulted transient extensional viscosities are presented in Figs. 6(c,d), which agree well with the simulated $\eta_E(t)$ data in the initial growing regime, but are of higher values in the steady state. Such overestimation of the steady-state extensional viscosities $\eta_E(\dot{\epsilon})$ is found for all extension rates we studied as shown in Fig. S10(b) of the SM. The quantitative difference between the decoupling approximations and the simulation data becomes smaller at high $\dot{\epsilon}$ when the chains are highly stretched.

C.   Steady-state behavior

The steady-state shear and planar extensional viscosities of the simulated systems are presented in Fig. 7, together with the zero-shear viscosities $\eta^+(t \to \infty)$ and zero-extension viscosities estimated by multiplying $\eta^+(t \to \infty)$ with the Trouton ratio $Tr = 4$ for Newtonian
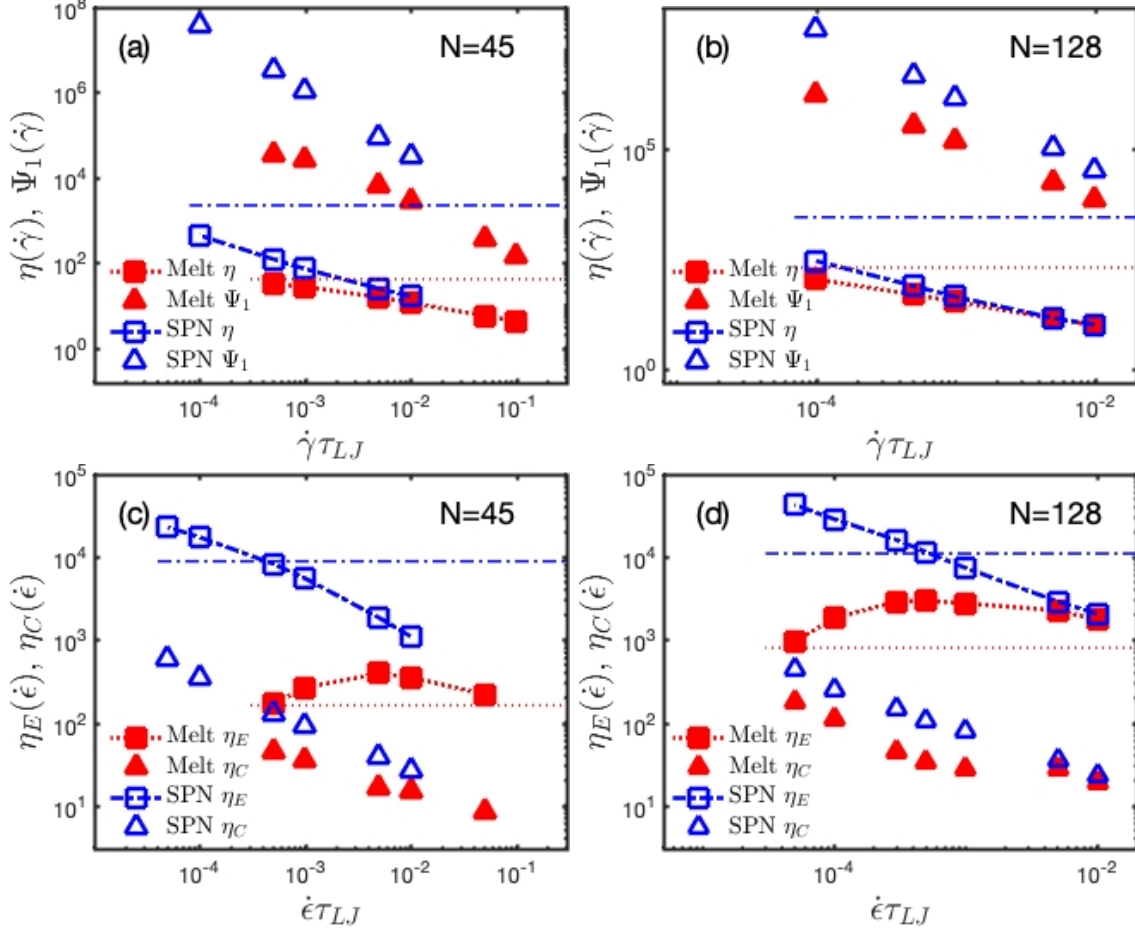
FIG. 7. (a,b) Steady-state shear viscosities $\eta(\dot{\gamma})$ and first normal stress coefficients $\Psi_1(\dot{\gamma})$ and (c,d) steady-state planar extensional and cross viscosities, $\eta_E(\dot{\epsilon})$ and $\eta_C(\dot{\epsilon})$, for the melt and SPN systems with two different chain lengths, respectively. The dotted and dotted-dashed horizontal lines in (a,b) are the zero-shear viscosities $\eta^+(t \to \infty)$ for the melts and SPNs, respectively, and those in (c,d) are the zero-extension viscosities estimated as $Tr\eta^+(t \to \infty)$ with the Trouton ratio $Tr = 4$.

fluids, i.e., $\eta_E^+(t \to \infty) = 4\eta^+(t \to \infty)$. For a given flow condition and given strain rate, the steady-state viscosity of a SPN is always higher than that of its melt counterpart. But the two sets of data approach each other with the increase of the strain rate. The Trouton ratio between the steady-state planar extensional and shear viscosities of a given system, $T_r = \eta_E(\dot{\epsilon})/\eta(\dot{\gamma})$ with $\dot{\epsilon} = \dot{\gamma}$, is much larger than that of the Newtonian fluid ($T_r = 4$) for all the strain rates studied in this work. For the unentangled melts with chain length $N = 45$, the Trouton ratio increases from $T_r \approx 5.4$ at $\dot{\epsilon} = \dot{\gamma} = 5 \times 10^{-4}\tau_{LJ}^{-1}$ to 38.9 at the strain

rate $5 \times 10^{-2} \tau_{LJ}^{-1}$, while that of the corresponding SPNs first increases from $Tr = 40.0$ at $\dot{\epsilon} = \dot{\gamma} = 10^{-4} \tau_{LJ}^{-1}$ to 77.9 at $10^{-3} \tau_{LJ}^{-1}$ and then decreases to 68.3 at $10^{-2} \tau_{LJ}^{-1}$. This reflects the different structural variation of the transient networks under shear and extensional flows. For the weakly entangled systems with $N = 128$, Tr of the melts increases from 16.8 at $\dot{\epsilon} = \dot{\gamma} = 10^{-4} \tau_{LJ}^{-1}$ to 176.2 at $10^{-2} \tau_{LJ}^{-1}$, while that of the SPNs increases from 94.5 at the strain rate $10^{-4} \tau_{LJ}^{-1}$ to 199.4 at $5 \times 10^{-3} \tau_{LJ}^{-1}$.

The simulation results in Figs. 7 (a, b) show clear steady-state shear-thinning behavior in both the melt and SPN systems where the shear viscosities $\eta(\dot{\gamma})$ are lower than the zero-shear values and decrease monotonically with the shear rate $\dot{\gamma}$. Similar behavior is found for the first normal stress coefficients $\Psi_1(\dot{\gamma})$. For polymeric liquids, the steady-state η frequently demonstrates a power law dependence on $\dot{\gamma}$ in the shear-thinning region, i.e., $\eta \sim \dot{\gamma}^{-\beta}$. Colby *et al.* suggested an exponent of $\beta = 1/2$ for unentangled polymer melts and concentrated solutions by using a scaling-level calculation based on the Rouse model and shear-rate dependence of the Pincus blob size [59]. They verified this 1/2 power law using experimental data collected from unentangled polystyrene (PS) melts and semidilute solutions of polyelectrolytes. Kröger *et al.* performed NEMD simulations using the same KG bead-spring model as employed in this work for chain lengths $N = 4-400$ over a broad range of shear rates [42]. Their simulation systems showed the general shear thinning behavior with $\eta(\dot{\gamma})$ approaching a universal power law independent of N. The power law exponent was given as $\beta = 0.60 \pm 0.10$. Our simulation results on $\eta(\dot{\gamma})$ of the melts with $N = 45$ and 128 fall very well onto Kröger's data, as shown in Fig. S11 of the SM. Power law fitting to each individual set of data at $Wi_M > 1$ (i.e., $\dot{\gamma}\tau_{LJ} > 10^{-3}$ for $N = 45$ and $\dot{\gamma}\tau_{LJ} > 10^{-4}$ for $N = 128$) renders $\beta = 0.43 \pm 0.02$ for the melts with $N = 45$ and $\beta = 0.54 \pm 0.02$ for $N = 128$, respectively, where the error bars measure the standard errors of the fitted exponent values. These β values are close to the experimental value (0.5) reported by Colby *et al.* [59]. The discrepancy of $\beta = 0.43$ obtained at $N = 45$ from the general power law given by Kröger [42] may be related to the range of data points available or way of fitting.

The $\eta(\dot{\gamma})$ and $\Psi_1(\dot{\gamma})$ results of the SPN systems decay with the shear rate faster than their melt counterparts. Power law fitting to the $\eta(\dot{\gamma})$ data points at $\dot{\gamma}\tau_{LJ} > 10^{-4}$ ($Wi_S > 26.3$) renders an exponent $\beta = 0.68 \pm 0.03$ for both chain lengths. The higher decay rate of the steady-state shear viscosities of the SPNs can be related to the shear-induced reduction in the average fraction of fully associated stickers as shown in Figs. 8(a) and 9(a). This

fraction decreases from around 95% in equilibrium and at very low shear rates to around or less than 80% at the highest $\dot{\gamma}$ studied in each system. In the mean time the fractions of the partially-reacted and open stickers grow with $\dot{\gamma}$, indicating that the number density of bridging or elastically active strands in the transient networks is reduced with the increase of $\dot{\gamma}$, see Fig. S7 of the SM. Furthermore Fig. 8(c) shows that the average sticky bond lifetime $\tau_b(\dot{\gamma})$ in steady state stays nearly constant over the range of $\dot{\gamma}$ studied, but the average partner exchange time $\tau_{pe}(\dot{\gamma})$ drops for more than one order of magnitude. It means that with the increase of $\dot{\gamma}$ the stickers are experiencing less number of association/dissociation events with their old partners before joining new partners and so moving more frequently from one sticker cluster to another cluster. This facilitates the release of chain deformation and consequently the stored stress. The faster decay of $\eta(\dot{\gamma})$ in the SPNs than in the melts thus originates from two extra stress relaxation mechanisms: the flow-induced reduction in the number density of elastically active strands and the increment in the frequency for the stickers to move from one sticker cluster to another.

The monotonic decrease of the fraction of fully reacted stickers in Figs. 8(a) and 9(a) indicates that the mechanism of shear-enhanced sticker reassociation rate, as proposed for interpreting the shear thickening behavior in dilute solutions of associative polymers [15, 16, 19, and 32], does not exist in concentrated or melt systems of associative telechelic chains. For the SPNs formed at high polymer concentrations and high sticker association energies, the majority (up to 95%) of the stickers are fully associated in equilibrium state or at very low shear rates. Increasing the shear rate can only lead to reduction in the fraction of fully associated stickers. Even though the average magnitudes of the chain stretching and reorientation still increase with increasing $\dot{\gamma}$, as shown in Figs. 9(c, d), their contributions to the steady-state shear and first normal stresses are counter-balanced by the reduction in the density of elastically active strands in the transient networks and the increment in the sticker partner exchange frequency. These systems can only undergo steady-state shear thinning, as have also been observed in experiments [15, 19, and 20].

On the other hand, the steady-state planar extensional viscosities, $\eta_E(\dot{\epsilon})$, of the un-entangled and weakly entangled polymer melts presented in Figs.7(c, d) demonstrate clear extension hardening behavior. Such extension hardening was not observed for well-entangled polymers at $Wi_R > 1$, but is pronounced in the systems composed of unentangled to mildly entangled chains as found in experiments [82 and 83] and atomistic simulations [84]. For

example, the polystyrene melt with $Z \approx 3.9$ entanglements per chain studied by Nielsen *et al.* showed extension hardening at intermediate Deborah numbers, $1 < De = \dot{\epsilon}\tau_d < 10$, with the maximum of η_E located at $De \approx 3$ [82]. They interpreted this phenomenon as the combined effect of anisotropic drag imposed by the surrounding chains and chain finite extensibility.

Recently Matsumiya *et al.* investigated the nonlinear elongational rheology of unentangled polystyrene (PS27) and poly(p-tert-butylstyrene) (PtBS53) melts [85]. For both materials, the steady-state elongational viscosities were found to exhibit strain-rate-hardening with maximum values at $Wi \geq 0.3$ and then undergo strain-rate softening with increasing $\dot{\epsilon}$. The hardening was attributed to the finite extensible nonlinear elasticity of the polymer chains and the softening was suggested to result from the suppression of the FENE effects due to reduced segment friction coefficient of highly stretched and oriented chains. Our simulation data on $\eta_E(\dot{\epsilon})$ of the melts in Figs. 7(c, d) are qualitatively consistent with their experimental results. In our simulations the maxima of η_E are found at $\dot{\epsilon}\tau_{LJ} \approx 5 \times 10^{-3}$ and 5×10^{-4} ($Wi_M \approx 6.1$ and 12.2) for the melts with chain lengths $N = 45$ and 128, respectively. The maximum steady-state extensional viscosity thus appears at lower $\dot{\epsilon}$ for melts with longer chains, which agrees with experimental observation [82]. The quantitative differences in the locations (measured in Weissenberg number) and relative heights of the η_E maxima between the simulation and experimental results can be related to the observation of Matsumiya *et al.* [85] that the exact extension hardening and softening behavior of a polymer melt will depend on the chemical structure of the constituent chains. The bulkiness of the monomers and the stiffness of the chains can all affect the magnitude of the segment friction reduction [86]. In experiments the PtBS chains show stronger hardening at intermediate Wi and weaker softening at higher Wi than the PS chains, which were proposed to result from the bulky side groups of PtBS that effectively screen the packing interactions between the backbone segments and so weaken the friction reduction [85].

The coarse-grained bead-spring chain model we employed does not take into account the chemical details. To examine the effect of bulkiness and stiffness, it is more convenient to vary the chain stiffness measured by the Flory characteristic ratio C_∞, or equivalently the Kuhn length $l_k = C_\infty l$ with l the backbone bond length. This will consequently alter the packing length that is proportional to the ratio between the monomer bulkiness (molecular weight per backbone bond m_0) and the chain stiffness as $p = M/\rho_0 N_{av} R^2 = (1/\rho_0 N_{av})m_0/C_\infty l^2$

where M and R are the molecular weight and average end-to-end distance of the polymer chain, N_{av} the Avogadro's number and ρ_0 the density of the melt. In simulations using the bead-spring chain model, the packing length can be calculated by $p = 1/\rho_{chain}R^2$ where ρ_{chain} is the polymer chain number density [87]. The characteristic ratio and packing length of the flexible KG chain model we used are $C_\infty = 1.82$ ($l_k \approx 1.75\sigma_{LJ}$) and $p \approx 0.68\sigma_{LJ}$, respectively [87]. O'Connor $et\ al.$ have performed nonlinear extensional flow simulations of entangled polymer melts using semi-flexible KG bead-spring chains with two different chain stiffness $C_\infty = 2.8$ and 2.2 ($l_k \approx 2.75\sigma_{LJ}$ and $2.11\sigma_{LJ}$) [44], and the corresponding packing lengths would be around $0.43\sigma_{LJ}$ and $0.56\sigma_{LJ}$, respectively [87]. The hardening regions found in their simulations span much wider ranges of Wi_R than the experimental data obtained from PS melts with similar numbers of entanglements. For their simulation systems with $Z = 4 \sim 9$ the hardening regions extend beyond $Wi_R = 30 \sim 40$, which is similar to our results in Fig. 7(d) for the melts with $N = 128$. For a given number of entanglements Z, the relative height of the maximum η_E was shown to decrease with the increase of chain stiffness and its location also shifts to lower Wi_R. Since the packing length $p \propto C_\infty^{-1}$ for fixed monomer size, these results imply stronger extensional hardening behavior with the increase of the packing length. This is qualitatively consistent with the experimental observation of Matsumiya $et\ al.$ [85] where the packing length $p \approx 0.585nm$ of the bulkier PtBS is larger than $p \approx 0.36nm$ of PS [88]. After the extension hardening region, the simulation results show that the longest chains begin extension thinning at the lowest Wi_R and have the largest drop in viscosity [44]. A more systematic investigation on the influence of the chain length and chemical structures, including stiffness and bulkiness, on the segment friction and consequently the extension hardening behavior will be left for further study.

In Figs. 7(c, d), the $\eta_E(\dot\epsilon)$ data of the SPNs obtained at small $\dot\epsilon$ are larger than the zero-extension viscosities $4\eta^+(t \to \infty)$, indicating the occurrence of steady-state extension hardening in these systems. But the range of extension rates we simulated with the lowest $\dot\epsilon = 5 \times 10^{-5}\tau_{LJ}^{-1} \gg 1/\tau_{d,S}$ could not capture the maxima of $\eta_E(\dot\epsilon)$, so the simulation data only demonstrate the extension softening behavior after passing the maxima. Similar to the shear-thinning case, these $\eta_E(\dot\epsilon)$ results have a power law dependence on $\dot\epsilon$, $\eta_E \sim \dot\epsilon^{-\beta}$. The exponent β is found to be around 0.57 ± 0.04 for the SPNs with $N = 45$ and 0.58 ± 0.02 for those with $N = 128$ by power law fitting to data points at $\dot\epsilon\tau_{LJ} > 10^{-4}$.
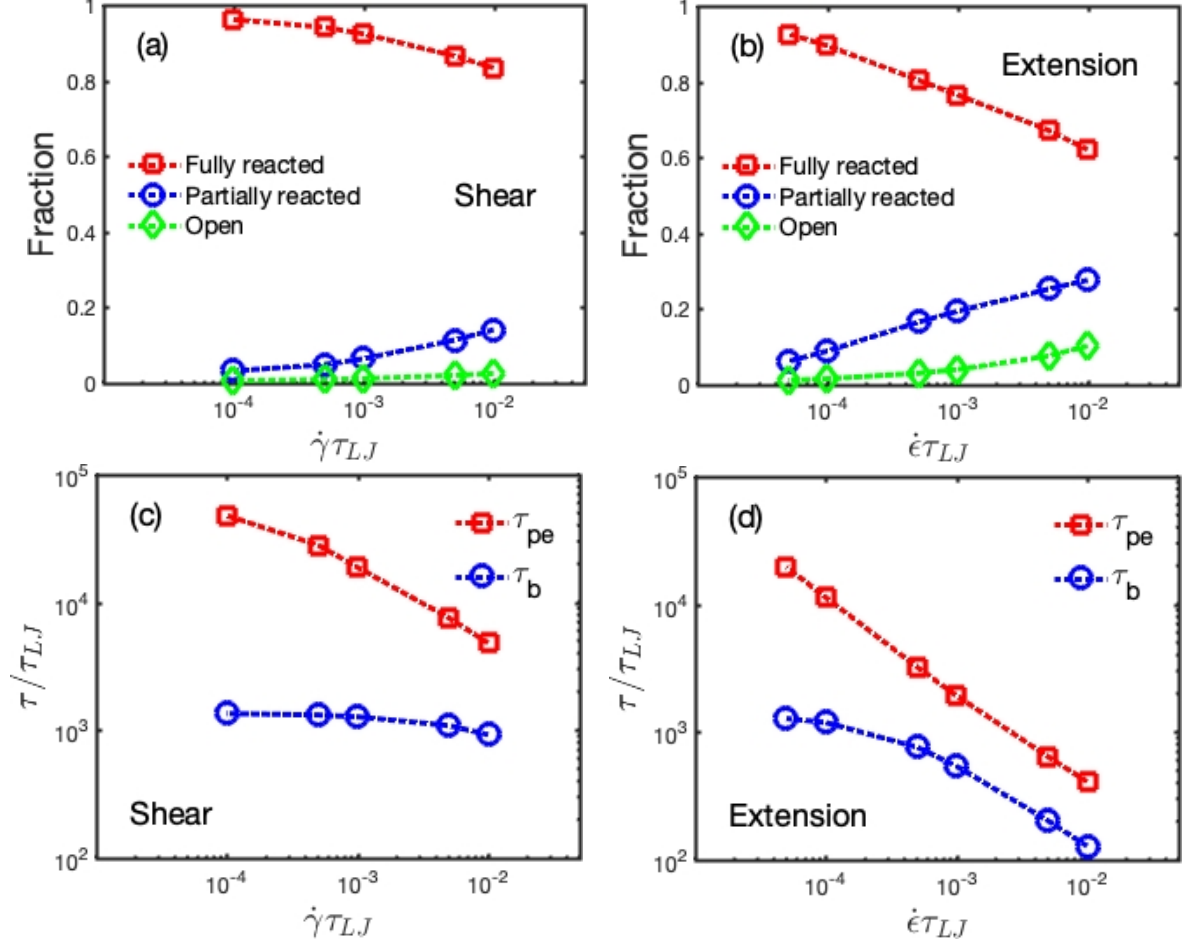
33

FIG. 8. (a,b) Steady-state fractions of open, partially- and fully-reacted sticker, and (c,d) average sticky bond lifetimes τ_b and partner exchange times τ_{pe} in the SPNs with chain length $N = 45$ under shear and extensional flows.

The steady-state extensional behavior of the studied polymer systems can also be interpreted using the flow-induced chain stretching, chain/segment orientation and sticker association/dissociation. In Figs. 9 (c,d), the steady-state chain stretching ratio $\lambda(\dot{\epsilon})$ of the melts with $N = 128$ first grows quickly with increasing $\dot{\epsilon}$, accompanied by the fast decay of the chain end-to-end vector orientation angle $\Theta_{ee}(\dot{\epsilon})$, leading to the extension hardening behavior observed in Fig. 7(d). At high extension rates, the chains are stretched towards their extensibility limit and also nearly fully aligned with the elongation direction. This may result in the theoretically proposed reduction of the segment friction and so the extension softening [82, 85, and 86]. For the SPNs with $N = 128$, the magnitudes of the chain stretching and orientation are already relatively high at small extension rates due to the chain
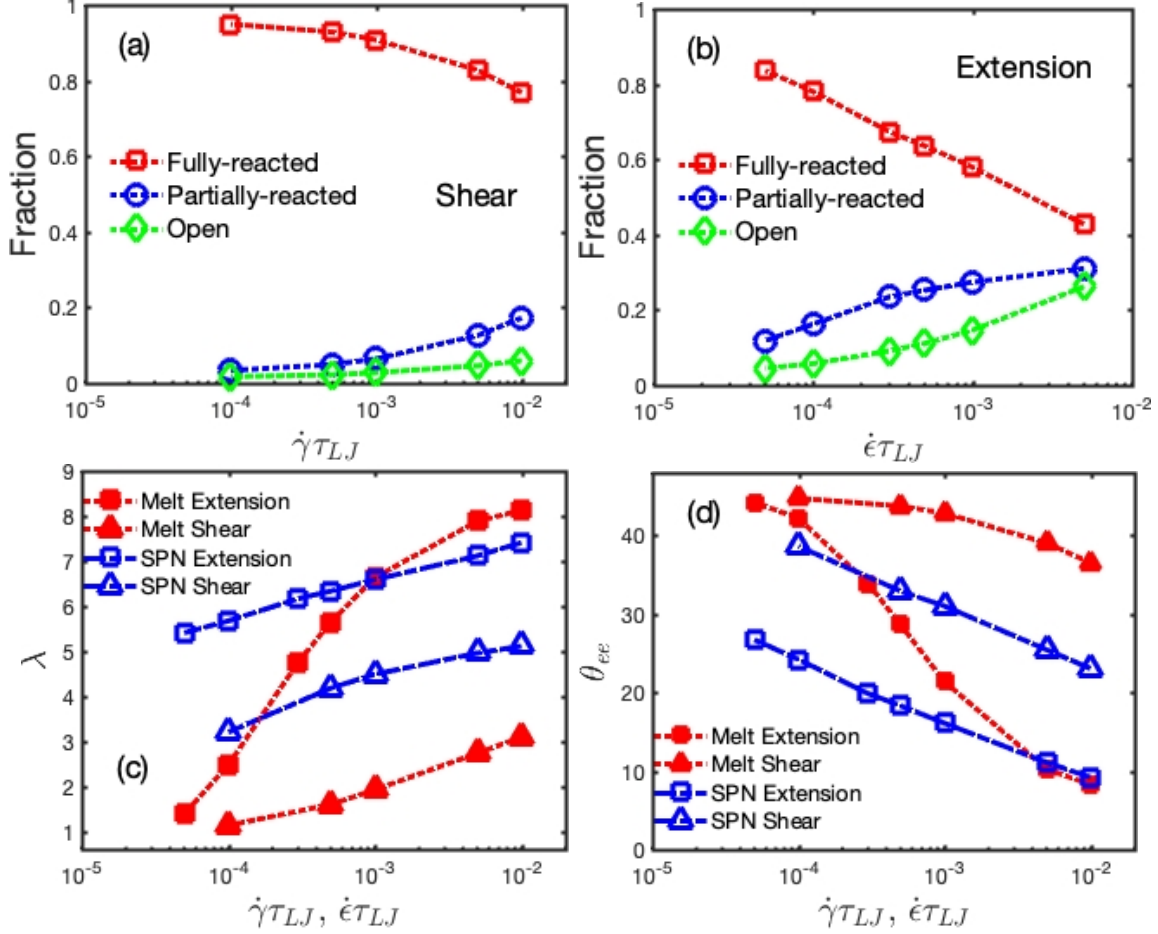
34

FIG. 9. (a,b) Steady-state fractions of open, partially- and fully-reacted stickers, (c) average chain stretching ratios λ, and (d) average chain end-to-end vector orientation angles with respect to the shear or elongation directions Θ_{ee} in the SPNs with chain length $N = 128$ under steady shear and extensional flows. In (c,d) the simulation results of their melt counterparts are also included.

cross-linking. They show weaker $\dot{\epsilon}$ dependence than those of the melt counterparts. In the mean time, Fig. 9(a) shows a quick drop of the average fraction of fully reacted stickers by nearly 40% over the range of $\dot{\epsilon}$ we studied. The sticker association behavior is also strongly affected by the extension flow. As shown in Fig. 8(d) for the unentangled SPNs, the average steady-state bond lifetime $\tau_b(\dot{\epsilon})$ drops by about one order of magnitude and the average sticker partner exchange time $\tau_{pe}(\dot{\epsilon})$ decreases by nearly two orders of magnitude over the range of $\dot{\epsilon}$ we studied. The significantly reduced sticky bond lifetimes, but enhanced partner exchange frequencies, coupled with the reduction in the number density of elastically active strands, give rise to the extension softening of the SPNs shown in Figs. 7(c, d).

Fig. 9(c) shows that at high extension rates the average steady-state chain stretching ratios λ in the melts are larger than those in the SPNs. This can be understood from the much broader probability distribution $P(R_{ee})$ of the chain end-to-end distances in the SPNs, spanning from $R_{ee} \sim \sigma_{LJ}$ for looping chains to $R_{ee} \sim N\sigma_{LJ}$ for fully stretched bridging chains, than that of the melts where nearly all chains are highly stretched, see Fig. S8 and discussions in Section S5 of the SM. In the SPNs the associated chains with small R_{ee} values are taking piecewise-stretched bending or folding configurations rather than compact coil conformations, which is verified in Fig. S9 by the agreement between the simulations results on the average steady-state chain segment stretching ratios and end-to-end vector orientation angles obtained from the melt and SPN systems at high $\dot{\epsilon}$. The contributions from such piecewise-stretched chains to the tensile stress are not sufficiently reflected in the average chain stretching ratio λ. In addtion there are also a number of bridging chains in the SPNs that are stretched to R_{ee} values higher than any of the non-associative chains in the melts. Therefore the steady-state extensional viscosity of the SPNs can still be larger than their melt counterparts, despite the average chain stretching ratios of the former could be smaller.

IV.   CONCLUSIONS

The nonlinear rheological and dynamic behavior of model supramolecular polymer networks and their non-associative polymer melt counterparts under shear and extension flows are studied by nonequilibrium hybrid molecular dynamics/Monte Carlo simulations. The supramolecular polymer networks are formed by associative telechelic chains with strong sticky bonding energy of $\varepsilon = 10k_BT$. In equilibrium state or at very low strain rates, about 95% of stickers in such transient networks are fully associated. Compared with the non-associative polymer melts, the SPN systems exhibit much stronger transient and steady-state rheological properties owing to the formation of reversible sticky bonds. In startup shear the SPNs demonstrate a transient strain hardening behavior at high shear rates, which does not exist in their melt counterparts. The growth of the shear stress above the linear viscoelastic envelope can be attributed to the shear-induced non-Gaussian chain stretching and reorientation of chain segments along the shear direction. In startup planar extensional flows, the polymer chains are subject to stronger stretching and reorientation effects than

those under shear flows at the same strain rates. The transient extensional viscosities of both the melt and SPN systems demonstrate strong strain hardening behavior over nearly the entire range of extension rates studied in this work. The transient shear and extensional tensile stresses of the SPN systems are found to undergo overshoot by growing up to a maximum value and then decreasing before entering the steady state. The decrease in the transient stresses can be attributed to the flow-induced reduction in the fraction of fully associated stickers and consequently the decrease in the number density of elastically active strands in the transient networks. At small strain rates, the decrease in the number of associated stickers only results from the flow-induced reduction in the probability of the stickers to reassociate with their old partners and so an increment in the frequency for them to move from one sticker cluster to another, while at high strain rates the effect of the reduced average sticky bond lifetime becomes important.

In steady state, the shear viscosities and first normal stress coefficients of both the melt and SPN show shear thinning behavior in consistence with published experimental and simulation results. The power law dependence of the shear viscosities on the shear rates obtained in our melts agree well with existing experimental and simulation works. In the SPNs, two extra stress relaxation mechanisms, namely the flow-induced reduction in the number density of elastically active strands and the increment in the frequency for the stickers to move from one sticker cluster to another, lead to faster decay of the shear viscosities of the SPNs with shear rate than those in their melt counterparts. On the other hand, the unentangled and weakly entangled melt and SPN systems we studied demonstrate steady-state extension hardening bahvior with the extensional viscosities obtained at lower extension rates going above the zero-extension viscosities, which again in qualitative agreement with experimental and simulation works using similar chain lengths. In the melts the extension flow induces strong chain stretching and orientation along the elongation direction, which results in the extension hardening. But at high extension rates, the highly stretched and orientated chains may effectively lead to reduction in the segment friction and consequently the extension softening behavior. In the SPNs the effects of flow-induced chain stretching and orientation are counter-balanced by the reduction in the average sticky bond lifetimes and the increment in the frequency of sticker partner exchange events, which together with the flow-induced reduction in the number density of elastically active strands in the transient networks, result in fast decay of the extensional viscosities in the extension softening region.

The agreement of our simulation results with relevant experimental works indicates that the nonequilibrium simulation methods we used can be further applied to study the flow behavior of dilute solutions of associative telechelic chains and the nonlinear rheological properties of supramolecular networks formed by polymer chains with multiple association groups per chain. The obtained microscopic information on the flow-induced chain stretching and local segment reorientation as well as the strain-rate dependence of the fractions of associated stickers and the characteristic lifetimes of sticky bonds can make significant contributions to examining the theoretical assumptions and developing more quantitative theoretical models for describing the nonlinear rheological and dynamic behavior of supramolcular polymer networks.

SUPPLEMENTARY MATERIAL

The supplementary material (SM) is available free of charge via Internet.

ACKNOWLEDGMENTS

REFERENCES

[1] M. J. Serpe and S. L. Craig, "Physical organic chemistry of supramolecular polymers," Langmuir **23**, 1626–1634 (2007).

[2] P. Cordier, F. Tournilhac, C. Soulié-Ziakovic, and L. Leibler, "Self-healing and thermoreversible rubber from supramolecular assembly," Nature **451**, 977–980 (2008).

[3] T. F. A. de Greef and E. W. Meijer, "Materials science - supramolecular polymers," Nature **453**, 171–173 (2008).

[4]J. A. Syrett, C. R. Becer, and D. M. Haddleton, "Self-healing and self-mendable polymers," Polym. Chem. **1**, 978–987 (2010).

[5]S. Seiffert and J. Sprakel, "Physical chemistry of supramolecular polymer networks," Chem. Soc. Rev. **41**, 909–930 (2012).

[6]A. Eisenberg, B. Hird, and R. B. Moore, "A new multiplet-cluster model for the morphology of random ionomers," Macromolecules **23**, 4098–4107 (1990).

[7]K. Yamauchi, J. Lizotte, and T. Long, "Thermoreversible poly(alkyl acrylates) consisting of self-complementary multiple hydrogen bonding," Macromolecules **36**, 1083–1088 (2003).

[8]D. Xu and S. L. Craig, "Multiple dynamic processes contribute to the complex steady shear behavior of cross-linked supramolecular networks of semidilute entangled polymer solutions," J. Phys. Chem. Lett. **1**, 1683–1686 (2010).

[9]K. E. Feldman, M. J. Kade, E. W. Meijer, d. C. J. Hawker, and E. J. Kramer, "Model transient networks from strongly hydrogen-bonded polymers," Macromolecules **42**, 9072–9081 (2009).

[10]M. Ahmadi, L. G. D. Hawke, H. Goldansaz, and E. van Ruymbeke, "Dynamics of entangled linear supramolecular chains with sticky side groups: influence of hindered fluctuations," Macromolecules **48**, 7300–7310 (2015).

[11]Q. Chen, Z. Zhang, and R. H. Colby, "Viscoelasticity of entangled random polystyrene ionomers," J. Rheol. **60**, 1031–1040 (2016).

[12]C. E. Williams, T. P. Russell, R. Jerome, and J. Horrion, "Ionic aggregation in model ionomers," Macromolecules **19**, 2877–2884 (1986).

[13]M. Müller, A. Dardin, U. Seidel, V. Balsamo, B. Ivan, H. Spiess, and R. Stadler, "Junction dynamics in telechelic hydrogen bonded polyisobutylene networks," Macromolecules **29**, 2577–2583 (1996).

[14]M. Rubinstein and A. Dobrynin, "Solutions of associative polymers," Trends In Polym. Sci. **5**, 181–186 (1997).

[15]S. X. Ma and S. L. Cooper, "Shear thickening in aqueous solutions of hydrocarbon end-capped poly(ethylene oxide)," Macromolecules **34**, 3294–3301 (2001).

[16]A. Tripathi, K. C. Tam, and G. H. McKinley, "Rheology and dynamics of associative polymers in shear and extension: Theory and experiments," Macromolecules **39**, 1981–1999 (2006).

[17]S. Burattini, H. M. Colquhoun, J. D. Fox, D. Friedmann, B. W. Greenland, P. J. F. Harris, W. Hayes, M. E. Mackay, and S. J. Rowan, "A self-repairing, supramolecular polymer system: healability as a consequence of donor-acceptor pi-pi stacking interactions," Chem. Commun. , 6717–6719 (2009).

[18]S. Suzuki, T. Uneyama, T. Inoue, and H. Watanabe, "Nonlinear rheology of telechelic associative polymer networks: shear thickening and thinning behavior of hydrophobically modified ethoxylated urethane (HEUR) in aqueous solution," Macromolecules **45**, 888–898 (2012).

[19]S. Suzuki, T. Uneyama, and H. Watanabe, "Concentration dependence of nonlinear rheological properties of hydrophobically modified ethoxylated urethane aqueous solutions," Macromolecules **46**, 3497–3504 (2013).

[20]T. Yan, K. Schröer, F. Herbst, W. H. Binder, and T. Thurn-Albrecht, "What controls the structure and the linear and nonlinear rheological properties of dense, dynamic supramolecular polymer networks?" Macromolecules **50**, 2973–2985 (2017).

[21]M. Rubinstein and A. N. Semenov, "Dynamics of entangled solutions of associating polymers," Macromolecules **34**, 1058–1068 (2001).

[22]R. Colby, X. Zheng, M. Rafailovich, J. Sokolov, D. Peiffer, S. Schwarz, Y. Strzhemechny, and D. Nguyen, "Dynamics of lightly sulfonated polystyrene ionomers," Phys. Rev. Lett. **81**, 3876–3879 (1998).

[23]Q. Chen, G. J. Tudryn, and R. H. Colby, "Ionomer dynamics and the sticky Rouse model," J. Rheol. **57**, 1441–1462 (2013).

[24]B. J. Gold, C. H. Hovelmann, N. Luhmann, N. K. Szekely, W. Pyckhout-Hintzen, A. Wischnewski, and D. Richter, "Importance of compact random walks for the rheology of transient networks," Acs Macro Lett. **6**, 73–77 (2017).

[25]E. B. Stukalin, L.-H. Cai, N. A. Kumar, L. Leibler, and M. Rubinstein, "Self-healing of unentangled polymer networks with reversible bonds," Macromolecules **46**, 7525–7541 (2013).

[26]D. Amin, A. E. Likhtman, and Z. Wang, "Dynamics in supramolecular polymer networks formed by associating telechelic chains," Macromolecules **49**, 7510–7524 (2016).

[27]F. Tanaka and S. Edwards, "Viscoelastic properties of physically cross-linked networks - transient network theory," Macromolecules **25**, 1516–1523 (1992).

[28] G. Marrucci, S. Bhargava, and S. L. Cooper, "Models of shear-thickening behavior in physically cross-linked networks," Macromolecules **26**, 6483–6488 (1993).

[29] A. N. Semenov and M. Rubinstein, "Dynamics of entangled associating polymers with large aggregates," Macromolecules **35**, 4821–4837 (2002).

[30] T. Uneyama, S. Suzuki, and H. Watanabe, "Concentration dependence of rheological properties of telechelic associative polymer solutions," Phys. Rev. E **86**, 031802 (2012).

[31] T. Annable, R. Buscall, and R. Ettelaie, "Network formation and its consequences for the physical behaviour of associating polymers in solution," Colloid Surf. A-Physicochem Eng. Asp. **112**, 97–116 (1996), Associating Polymers 1995 Meeting, Loen, Norway, 1995.

[32] K. Tam, R. Jenkins, M. Winnik, and D. Bassett, "A structural model of hydrophobically modified urethane-ethoxylate (HEUR) associative polymers in shear Flows," Macromolecules **31**, 4149–4159 (1998).

[33] D. Xu, C.-Y. Liu, and S. L. Craig, "Divergent shear thinning and shear thickening behavior of supramolecular polymer networks in semidilute entangled polymer solutions," Macromolecules **44**, 2343–2353 (2011).

[34] G. W. Park and G. Ianniruberto, "A new stochastic simulation for the rheology of telechelic associating polymers," J. Rheol. **61**, 1293–1305 (2017).

[35] F. Zhuge, L. G. D. Hawke, C.-A. Fustin, J.-F. Gohy, and E. van Ruymbeke, "Decoding the linear viscoelastic properties of model telechelic metallo-supramolecular polymers," J. Rheol. **61**, 1245–1262 (2017).

[36] L. Pellens, R. Corrales, and J. Mewis, "General nonlinear rheological behavior of associative Polymers," J. Rheol. **48**, 379–393 (2004).

[37] J. Sprakel, E. Spruijt, M. A. C. Stuart, N. A. M. Besseling, M. P. Lettinga, and J. van der Gucht, "Shear banding and rheochaos in associative Polymer networks," Soft Matter **4**, 1696–1705 (2008).

[38] T. Witten and M. Cohen, "Cross-linking in shear-thickening ionomers," Macromolecules **18**, 1915–1918 (1985).

[39] A. Vaccaro and G. Marrucci, "A model for the nonlinear rheology of associating polymers," J. Non-Newton Fluid **92**, 261–273 (2000).

[40] Y. Serero, V. Jacobsen, J. Berret, and R. May, "Evidence of nonlinear chain stretching in the rheology of transient networks," Macromolecules **33**, 1841–1847 (2000).

[41] J. G. H. Cifre, T. Barenbrug, J. D. Schieber, and B. H. A. A. van den Brule, "Brownian dynamics simulation of reversible polymer networks under shear using a non-interacting dumbbell model," J Non-Newton Fluid **113**, 73–96 (2003).

[42] M. Kröger and S. Hess, "Rheological evidence for a dynamical crossover in polymer melts via nonequilibrium molecular dynamics," Phys. Rev. Lett. **85**, 1128–1131 (2000).

[43] P. J. Daivis, M. L. Matin, and B. D. Todd, "Nonlinear shear and elongational rheology of model polymer melts by non-equilibrium molecular dynamics," J. Non-Newton Fluid **111**, 1–18 (2003).

[44] T. C. O'Connor, N. J. Alvarez, and M. O. Robbins, "Relating chain conformations to extensional stress in entangled polymer melts," Phys. Rev. Lett. **121**, 047801 (2018).

[45] Z. Li, H. Djohari, and E. E. Dormidontova, "Molecular dynamics simulations of supramolecular polymer rheology," J. Chem. Phys. **133**, 184904 (2010).

[46] R. S. Hoy and G. H. Fredrickson, "Thermoreversible associating polymer networks. i. interplay of thermodynamics, chemical kinetics, and polymer physics," J. Chem. Phys. **131**, 224902 (2009).

[47] K. Kremer and G. S. Grest, "Dynamics of entangled linear polymer melts - a molecular-dynamics simulation," J. Chem. Phys. **92**, 5057–5086 (1990).

[48] Z. Wang, A. E. Likhtman, and R. G. Larson, "Segmental dynamics in entangled linear polymer melts," Macromolecules **45**, 3557–3570 (2012).

[49] C. C. Huang, H. Xu, and J. P. Ryckaert, "Kinetics and dynamic properties of equilibrium polymers," J. Chem. Phys. **125**, 094901 (2006).

[50] M. P. Allen and D. J. Tildesley, *Computer Simulation of Liquids* (Clarendon Press, Oxford, 1987).

[51] A. W. Lees and S. F. Edwards, "The computer study of transport processes under extreme conditions," Journal of Physics C: Solid State Physics **5**, 1921 (1972).

[52] A. M. Kraynik and D. A. Reinelt, "Extensional motions of spatially periodic lattices," Int. J. of Multiph. Flow **18**, 1045–1059 (1992).

[53] B. Todd and P. Daivis, "A new algorithm for unrestricted duration nonequilibrium molecular dynamics simulations of planar elongational Flow," Compu. Phys. Commun. **117**, 191–199 (1999).

[54] B. D. Todd and P. J. Daivis, "Homogeneous non-equilibrium Molecular dynamics Simulations of viscous Flow: techniques and applications," Molecular Simulation **33**, 189–229

(2007).

[55] D. J. Evans and G. P. Morris, *Statistical Mechanics of Nonequilibrium Liquids* (Academic Press, London, 1990).

[56] A. Baranyai and D. J. Evans, "New algorithm for constrained molecular-dynamics simulation of liquid benzene and naphthalene," Molecular Phys. **70**, 53–63 (1990).

[57] P. Daivis and B. Todd, "A simple, direct derivation and proof of the validity of the SLLOD equations of motion for generalized homogeneous flows," J. Chem. Phys. **124**, 194103 (2006).

[58] P. J. Daivis, M. L. Matin, and B. D. Todd, "Nonlinear shear and elongational rheology of model polymer melts at low strain rates," J. Non-Newton Fluid **147**, 35–44 (2007).

[59] R. H. Colby, D. C. Boris, W. E. Krause, and S. Dou, "Shear thinning of unentangled flexible polymer liquids," Rheol. Acta **46**, 569–575 (2007).

[60] A. E. Likhtman and T. C. B. McLeish, "Quantitative theory for linear dynamics of linear entangled polymers," Macromolecules **35**, 6332–6343 (2002).

[61] J. Cao and A. E. Likhtman, "Simulating Startup Shear of Entangled Polymer Melts," ACS Macro Lett. **4**, 1376–1381 (2015).

[62] J. Ramirez, S. K. Sukumaran, B. Vorselaars, and A. E. Likhtman, "Efficient on the fly calculation of time correlation functions in computer simulations," J. Chem. Phys. **133**, 154103 (2010).

[63] M. Doi and S. F. Edwards, *The theory of Polymer dynamics*, 1st ed. (Claredon Press, Oxford, 1988).

[64] P. G. de Gennes, "Reptation of a polymer chain in the presence of fixed obstacles," J. Chem. Phys. **55**, 572–579 (1971).

[65] R. S. Graham, A. E. Likhtman, T. C. B. McLeish, and S. T. Milner, "Microscopic theory of linear, entangled polymer chains under rapid deformation including chain stretch and convective constraint release," J. Rheol. **47**, 1171–1200 (2003).

[66] H. Watanabe, Y. Matsumiya, and T. Inoue, "Revisit the stress-optical rule for entangled flexible chains: overshoot of stress, segmental orientation, and chain stretch on start-up of flow," Nihon Reoroji Gakkaishi **43**, 105–112 (2015).

[67] Y. Masubuchi and H. Watanabe, "Origin of stress overshoot under start-up shear in primitive chain network simulation," ACS Macro Lett. **3**, 1183–1186 (2014).

[68] M. H. N. Sefiddashti, B. J. Edwards, and B. Khomami, "Evaluation of reptation-based modeling of entangled polymeric fluids including chain rotation via nonequilibrium molecular dynamics simulation," Physical Review Fluids **2**, 083301 (2017).

[69] S. Costanzo, Q. Huang, G. Ianniruberto, G. Marrucci, O. Hassager, and D. Vlassopoulos, "Shear and extensional rheology of polystyrene melts and solutions with the same number of entanglements," Macromolecules **49**, 3925–3935 (2016).

[70] E. Menezes and W. Graessley, "Non-linear rheological behavior of polymer systems for several shear-flow histories," J. Polym. Sci. Part B - Polym. Phys. **20**, 1817–1833 (1982).

[71] D. Auhl, J. Ramirez, A. E. Likhtman, P. Chambon, and C. Fernyhough, "Linear and nonlinear shear flow behavior of monodisperse polyisoprene melts with a large range of molecular weights," J. Rheol. **52**, 801–835 (2008).

[72] J. Kim, B. Edwards, D. Keffer, and B. Khomami, "Single-chain dynamics of linear polyethylene liquids under shear flow," Physics Letters A **373**, 769 – 772 (2009).

[73] M. H. N. Sefiddashti, B. J. Edwards, and B. Khomami, "Individual chain dynamics of a polyethylene melt undergoing steady shear flow," J. Rheol. **59** (2015).

[74] M. Rubinstein and R. H. Colby, *Polymer Physics*, 1st ed. (Oxford University Press, Oxford New York, 2003).

[75] A. Cohen, "A Pade approximant to the inverse Langevin function," Rheol. Acta **30**, 270–273 (1991).

[76] R. Jedynak, "Approximation of the inverse Langevin function revisited," Rheol. Acta **54**, 29–39 (2015).

[77] T. C. B. McLeish and R. G. Larson, "Molecular constitutive equations for a class of branched polymers: The pom-pom polymer," J. Rheol. **42**, 81–110 (1998).

[78] D. W. Mead, R. G. Larson, and M. Doi, "A molecular theory for fast flows of entangled polymers," Macromoleccules **31**, 7895–7914 (1998).

[79] C. J. S. Petrie, "Extensional viscosity: A critical discussion," J. Non-Newton Fluid **137**, 15–23 (2006).

[80] M. Wagner, H. Bastian, P. Hachmann, J. Meissner, S. Kurzbeck, H. Munstedt, and F. Langouche, "The strain-hardening behaviour of linear and long-chain-branched polyolefin melts in extensional Flows," Rheol. Acta **39**, 97–109 (2000).

[81] A. Shabbir, H. Goldansaz, O. Hassager, E. van Ruymbeke, and N. J. Alvarez, "Effect of Hydrogen Bonding on Linear and Nonlinear Rheology of Entangled Polymer Melts,"

Macromolecules **48**, 5988–5996 (2015).

[82]J. K. Nielsen, H. K. Rasmussen, O. Hassager, and G. H. McKinley, "Elongational viscosity of monodisperse and bidisperse polystyrene melts," J. Rheol. **50**, 453–476 (2006).

[83]S. L. Wingstrand, N. J. Alvarez, Q. Huang, and O. Hassager, "Linear and nonlinear universality in the rheology of polymer melts and solutions," Phys. Rev. Lett. **115**, 078302 (2015).

[84]C. Baig, B. Edwards, D. Keffer, H. Cochran, and V. Harmandaris, "Rheological and structural studies of linear polyethylene melts under planar elongational flow using nonequilibrium molecular dynamics simulations," J. Chem. Phys. **124**, 084902 (2006).

[85]Y. Matsumiya, H. Watanabe, Y. Masubuchi, Q. Huang, and O. Hassager, "Nonlinear elongational rheology of unentangled Polystyrene and Poly(p-tert-butylstyrene) melts," Macromolecules **51**, 9710–9729 (2018).

[86]G. Marrucci and G. Ianniruberto, "Interchain pressure effect in extensional flows of entangled polymer melts," Macromolecules **37**, 3934–3942 (2004).

[87]R. Everaers, S. K. Sukumaran, G. S. Grest, C. Svaneborg, and A. S. A. Kremer, "Rheology and microscopic topology of entangled polymeric liquids," Science **303**, 823–826 (2004).

[88]Q. Chen, Y. Matsumiya, Y. Masubuchi, H. Watanabe, and T. Inoue, "Dynamics of polyisoprene-poly(p-tert-butylstyrene) diblock copolymer in disordered state," Macromolecules **44**, 1585–1602 (2011).